This is a preprint, the final version is subject to change, of the American Mineralogist (MSA)
Cite as Authors (Year) Title. American Mineralogist, in press.
DOI: https://doi.org/10.2138/am-2020-7286

REVISION 1

Mg diffusion in forsterite from 1250-1600 °C

Michael C. Jollands[1,2], Irina Zhukova[1,3], Hugh St.C O'Neill[1], Jörg Hermann[1,4]

[1]Research School of Earth Sciences, Australian National University, 142 Mills Rd, ACT 0200, Australia.

[2]Institute of Earth Sciences, Géopolis Building, University of Lausanne, 1015 Lausanne, Switzerland.

[3]State Key Laboratory of Geological Processes and Mineral Resources, China University of Geosciences (Wuhan), 388 Lumo Rd, Hongshan, Wuhan, Hubei, China 430074

[4]Institute of Geology, University of Bern, Baltzerstrasse 1+3, 3012 Bern, Switzerland.

corresponding author: michael.jollands@unil.ch

Abstract

^{26}Mg tracer diffusion coefficients were determined in single crystals of pure synthetic forsterite (Mg_2SiO_4). Isotopically-enriched powder sources both acted as the ^{26}Mg source and buffered the activities of silica ($aSiO_2$) at forsterite+protoenstatite ($Mg_2Si_2O_6$) (high $aSiO_2$) and forsterite+periclase (MgO) (low $aSiO_2$). Experiments were conducted at atmospheric pressure between 1250 and 1600 °C, and at oxygen fugacities (fO_2s) between 10^{-12} bars (CO-CO_2 mix) and $10^{-0.7}$ bars (air). The resulting diffusion profiles were measured along the three principal crystallographic axes (*a*, *b* and *c*; ||[100], ||[010], ||[001]) using laser-ablation inductively-coupled-plasma mass-spectrometry (LA-ICP-MS), with a quadrupole mass spectrometer. These

measurements were corroborated by ion microprobe using the Sensitive High Resolution Ion Microprobe-Reverse Geometry (SHRIMP-RG) instrument.

Mg tracer diffusion is anisotropic, with $D_{[001]}>D_{[010]}>D_{[100]}$, the difference in diffusion coefficients varying by about one order of magnitude at a given temperature with crystallographic orientation. Diffusion is faster in protoenstatite-buffered than periclase-buffered conditions, again with around one order of magnitude difference in diffusivity between buffering conditions. There is no apparent effect of fO_2 on diffusion. A global fit to all data, including data from Chakraborty et al. (1994) and Morioka (1981) yields the relationship:

$$\log_{10}D=\log_{10}D_0(m^2s^{-1})+0.61(\pm0.03)\log_{10}a_{SiO_2}+\frac{-359(\pm10)\ kJmol^{-1}}{2.303RT}$$

where $\log_{10}D_0$ is –3.15 (±0.08), -3.61 (±0.02) and -4.01 (± 0.05) m^2s^{-1} for the [001], [010] and [100] directions, respectively (1 s.d.). The LA-ICP-MS technique reproduces diffusion coefficients determined by SHRIMP-RG, albeit with slightly different absolute values of isotope ratios. This shows that LA-ICP-MS, which is both accessible and rapid, is a robust analytical method for such tracer diffusion studies.

Keywords: Diffusion, olivine, forsterite, magnesium, experimental petrology

Introduction

The prominence of olivine, $(Mg, Fe^{2+})_2SiO_4$, as the dominant mineral in the Earth's upper mantle, coupled with its experimental accessibility, has led to its transport properties being the most intensively studied of all silicate minerals. Diffusion especially has received much attention. Following several decades of research, there is generally good agreement that of the major elements in $(Mg,Fe^{2+})_2SiO_4$ olivine, Si diffusion is the slowest of the major elements (Bejina et al., 1999; Costa and

Chakraborty, 2008; Dohmen et al., 2002b; Fei et al., 2012), Mg self/tracer or Fe-Mg inter-diffusion (Chakraborty, 1997; Dohmen et al., 2007; Dohmen and Chakraborty, 2007, Buening and Buseck, 1973; Hier-Majumder et al., 2005; Wang et al., 2004) is the fastest, and O diffusion is intermediate (Ando et al., 1981; Dohmen et al., 2002b; Jaoul et al., 1980; Reddy et al., 1980). However, there still remain many contentious and important issues, including the effects of water (Costa and Chakraborty, 2008; Fei et al., 2018; Fei et al., 2013; Hier-Majumder et al., 2005; Wang et al., 2004), pressure (Bejina et al., 1999; Chakraborty et al., 1994; Fei et al., 2018), and silica activity (Zhukova et al., 2014) on diffusion, especially of trace-elements (Spandler and O'Neill 2010; Zhukova et al, 2017; Jollands et al. 2014, 2016).

From an experimental and analytical perspective, studies of diffusion in olivine have been central to developing and testing the advantages and drawbacks of different approaches and procedures. Experimental anneals to produce measurable diffusion profiles have employed diffusion couples consisting of crystal-melt (Jurewicz and Watson, 1988; Spandler and O'Neill, 2010); crystal-crystal (Chakraborty, 1997); crystal-polyphase powder (Jollands et al., 2014; Zhukova et al., 2014); crystal-film (Dohmen et al., 2002a); polycrystalline aggregates (Fei et al., 2018); crystal-fluid (Demouchy and Mackwell, 2003; Demouchy and Mackwell, 2006; Jollands et al., 2016b); and crystal-gas (e.g. Ryerson et al., 1989), while analytically the diffusion profiles have been measured using the electron microprobe (Chakraborty, 1997); Rutherford Backscattering Spectroscopy (Cherniak, 2010; Cherniak and Liang, 2014; Dohmen et al., 2007); Nuclear Reaction Analysis (Ryerson et al., 1989; Cherniak and Watson, 2012); LA-ICP-MS (Spandler and O'Neill, 2010; Spandler et al., 2007); SIMS depth-profiling (Ito and Ganguly, 2006) and Local Electrode Atom Probe

(LEAP; Bloch et al., 2019). Many of these approaches were developed, or refined, using natural or synthetic olivine of various compositions.

Diffusivities in crystals are sensitive to their point-defect structures, which in turn depend on their thermodynamic states. While the thermodynamic state of a crystal in a diffusion experiment would ideally be completely determined, this is impractical in most chemical diffusion experiments due to the large number of thermodynamic components present. It is feasible, however, in the study of tracer diffusion in forsterite, which exists in a three-component system, Mg-Si-O (barring considerations of isotopic components), so that the equilibrium thermodynamic state of the forsterite is uniquely defined by the coexistence of two additional phases. Here, we expand on previous studies (Andersson, 1987; Chakraborty et al., 1994; Fei et al., 2018; Morioka, 1981; Sockel et al., 1980) by reconsidering the effects of major-element chemical potentials (notably the activity of silica ($aSiO_2$)) on Mg tracer diffusion, defining the equilibrium thermodynamic state of forsterite using a gas phase (air or a CO-CO_2 mix) plus either MgO or an $Mg_2Si_2O_6$-pyroxene. We also demonstrate that laser-ablation inductively-coupled-plasma mass-spectrometry (LA-ICP-MS) with a simple quadrupole mass spectrometer, used previously for analysing trace-element diffusion profiles (e.g., Spandler and O'Neill 2010), can successfully measure experimental isotope diffusion profiles.

Methods

Experimental

Czochralski-grown single crystals of forsterite supplied by the Solix Corporation, Belarus, were cut into cubes of approximate dimension 2.5 x 2.5 x 2.5 mm. The cut surfaces were oriented parallel to the (001), (010) or (100) planes. Full trace-element contents of the forsterite from the same supplier are given in Zhukova et al. (2014);

the impurities include around 20-30 wt. ppm Al with <5 wt. ppm Fe. These cubes were mounted in epoxy and polished down to 1 μm diamond (cloth lap), then recovered from the resin for diffusion experiments. Further information regarding the experimental and analytical methodology is presented in Supplementary Figure 1. Isotopically-distinctive buffering phase assemblages were synthesised from ^{26}MgO (99.62% ^{26}Mg, obtained from Isoflex USA), mixed with reagent grade MgO and SiO_2 in proportions calculated to give either Mg_2SiO_4-$Mg_2Si_2O_6$ (forsterite-protoenstatite, herein fo-prEn) or Mg_2SiO_4-MgO (forsterite-periclase, herein fo-per) assemblages to buffer $aSiO_2$ (and aMgO). The mole fractions of each phase and by-weight isotopic enrichments were: fo-prEn: 43.1 mol% $Mg_2Si_2O_6$, 56.9 mol % Mg_2SiO_4, 44.7 wt. % ^{24}Mg, 5.7 wt. % ^{25}Mg, 49.6 wt. % ^{26}Mg (4.5x enrichment); fo-per: 32.9 mol% MgO, 67.1 mol % Mg_2SiO_4, 46.2 wt. % ^{24}Mg, 5.9 wt. % ^{25}Mg, 47.9 wt. % ^{26}Mg (4.3x enrichment). Relative isotopic abundances are calculated assuming both that the non-enriched MgO, and the remaining 0.38% of MgO in the enriched material has the natural abundances.

The mixes were ground under acetone in an agate mortar, pressed into pellets in a tungsten carbide dye and sintered in air at 1300 °C. These were then re-ground, mixed with polyethylene oxide glue and pasted onto polished surfaces of the forsterite crystals. The glue-powder-crystal assemblage was then dried for ~12 h at ~100 °C, then the crystals were placed onto a bed of non-isotopically-enriched MgO or Mg_2SiO_4-$Mg_2Si_2O_6$ (matched to the buffering assemblage adhered to the crystal) in a Pt crucible and annealed in either air in a high temperature box furnace or a gas-mixing furnace (O'Neill and Eggins 2002) under CO-CO_2 gas flow, to control the oxygen fugacity at lower values than that of air (see Table 1). Temperatures were

monitored and controlled using type B Pt-Rh thermocouples, with an estimated accuracy of 2 °C.

Following the diffusion anneals, the recovered crystals were mounted in epoxy on a plane perpendicular to the diffusion interface, ground down by around 500 µm, and polished with 6 µm then 3 µm diamond paste on cloth laps for LA-ICP-MS analysis. Some visible surface degradation always occurred. However, the roughness associated with this is <5 µm (an example experimental charge is shown in Figure 1 and Supplementary Figure 2), considerably shorter than the length scales of diffusion. For SHRIMP-RG analysis, several crystals were selected and cut from different mounts, remounted together in epoxy in one mount, and repolished. The mount was then degassed for ~100 hours in a vacuum oven at 60 °C and coated with 50 nm Au.

Analytical

LA-ICP-MS Measurements were conducted using a 193 nm LambdaPhysik Compex ArF excimer laser coupled to an Agilent 7700x quadrupole ICP-MS via He-Ar carrier gas. The laser beam was apertured to give an on-sample slit-shaped beam with approximate dimensions 6x100 µm, with the long axis parallel to the diffusion interface. The slit was scanned along the diffusion profile from low to high ^{26}Mg concentration (core to rim). The pulse rate was 5 Hz and laser energy was maintained at 50-60 mJ at point of exit. ^{24}Mg, ^{25}Mg and ^{26}Mg were counted for 0.1, 0.1 and 0.3 s per sweep, respectively. ^{29}Si was used as an internal standard (dwell time 0.01s) and ^{57}Fe and ^{27}Al (potential contaminants) counted for 0.05 s each. NIST 610 glass (Jochum et al. (2011) values) was used as the primary standard to quantify Fe and Al only – these data were reduced using Iolite freeware (Paton et al., 2011).

144 Isotopic concentrations of Mg (^{24}Mg, ^{25}Mg and ^{26}Mg) along the diffusion profiles
145 were extracted from the raw data in two ways. Firstly, data were converted to counts
146 per second, then background corrected and normalised to ^{29}Si, i.e.
147 ^{26}Mg(cps)/^{29}Si(cps). In lieu of a true external standard, a correction was applied using
148 the crystal core as an isotopic standard, assuming it has the natural isotope ratio
149 (modified from Longerich et al., 1996).

$$C^{x}Mg_{sample} = \frac{R^{x}Mg_{sample} C^{x}Mg_{core}}{R^{x}Mg_{core}} \quad (1)$$

150 Where C is the content (expressed as isotopic abundance, i.e. 0.1101 for ^{26}Mg) and R
151 is the Si-and background corrected count rate. Subscript 'core' represents a mean of
152 the 50 innermost points of the transect (around 25 μm), and 'sample' is the whole
153 profile. For the second reduction method, all above steps were done, then the fraction
154 of the isotope ^{x}Mg (x = 24, 25 or 26) was calculated from:

$$\frac{^{x}Mg}{\sum Mg} = \frac{^{26}Mg}{^{24}Mg + ^{25}Mg + ^{26}Mg} \quad (2)$$

155 Processed data are available in Supplementary dataset 1. Visual inspection of
156 comparisons of D for ^{26}Mg determined following the two different methods of data
157 reduction (either normalised, or not, to ∑Mg) suggest a good correlation
158 (Supplementary Figure 3). However, the reduced chi-squared (χ^2_ν) between a 1:1 line
159 and the data (determined using total least squares to account for uncertainties in x and
160 y, without incorporating the uncertainty on the interface position) is high (χ^2_ν=3.4 or
161 15.7, depending on whether eq. (3) or (5)is used), suggesting that the imposition of
162 the ∑Mg condition affects the Ds in a non-negligible way. This is likely due to ^{24}Mg
163 profiles being quite poorly resolved relative to ^{26}Mg profiles (probably a consequence

of short counting times), and showing resolvably (but not systematically so) different diffusivities (see Supplementary Figure 4 for more information). Therefore, we chose to not apply the $\Sigma Mg=^{24}Mg+^{25}Mg+^{26}Mg$ correction.

For each profile, the crystal-powder interface was located by inspection of the analytical data. This was generally done using the major drop in Si counts associated with the laser beam moving into the epoxy resin. In some cases, this was also associated with a large jump in Al and Fe counts, and/or a large change in slope of ^{26}Mg. The potential effect of this partially subjective choice of position is a function of the length of the diffusion profile and it is minimal with respect to the estimated diffusion coefficients associated with the profile lengths in this study. For example, a ~10 micron misplacement of the assigned interface, on a 150-200 μm long profile leads to ~0.05 logD unit variation (Supplementary Figure 5). This was also discussed by Zhukova et al. (2014), who concluded that the effect of changing the interface position, when converting time to distance during data processing, has a much larger effect on the interface concentration than the extracted diffusion coefficient.

SHRIMP-RG The reverse-geometry sensitive high-resolution ion microprobe (SHRIMP-RG) was used for secondary ion mass spectrometry (SIMS) measurements. Secondary ions were sputtered by an O^{2-} primary beam 5 μm in diameter. The 45° incidence angle of the primary beam in SHRIMP-RG results in a transformation of the analytical spot to a slightly elongated ellipse, hence samples were oriented such that the short axis of the ellipse was parallel to the diffusion direction to obtain the optimal spatial resolution. Following a two-minute raster of the beam over the sample to clean the surface, the nominal masses analysed were 24, 25 and 26 and 28, counted for 2, 2, 3 and 1 seconds, respectively.

189 The positions of the SHRIMP-RG spots were determined post-analysis by taking high
190 resolution photomicrographs and measuring distances from the interface using ImageJ
191 (Schindelin et al., 2015). Where spots overlapped, the spacing was assumed to be
192 equidistant between each analysis.
193 For the shortest profiles (<20 μm), the stage was moved 1 step (~3 μm) between each
194 analysis, such that adjacent analyses partially overlap. To determine if this overlap
195 affected the measured ratios, one profile (1250 °C, forsterite-periclase buffered
196 experiment) was measured both forwards (away from the interface) and backwards
197 (towards the interface).
198 The data were processed similarly to the LA-ICP-MS data, by normalising to ^{28}Si
199 then correcting to the natural ratio using the count rate ratio in the crystal core. Data
200 were either normalised or not to ∑Mg, as for the LA-ICP-MS data.
201 **Extraction of diffusion coefficients**
202 Two methods were used for extracting diffusion coefficients, with all fitting done
203 using non-linear least squares regression with MATLAB. Interpretation of the
204 observed diffusion profiles is complicated by the decrease of ^{26}Mg in the diffusant
205 source as it exchanges with Mg in the crystal, causing ^{26}Mg/ΣMg at the crystal
206 interface to decrease continuously during the diffusion anneal. Because of the large
207 number of profiles, and to reduce operator bias, all curve fitting was done
208 automatically. To enhance the probability of achieving global minima, multi-start
209 algorithms with at least ten random seeds were used, and all fits were visually
210 inspected.
211 Initially, all data were fitted to the constant diffusion coefficient, constant interface,
212 one dimensional, semi-infinite medium solution to Fick's second law (Crank, 1975),
213 i.e. fitting directly to an error function-shaped curve:

$$C(x,t)=(C_{rim}-C_{core}).\mathrm{erfc}\left(\frac{x}{\sqrt{4Dt}}\right)+C_{core} \quad (3)$$

where C_{rim} and C_{core} are the concentrations at the interface and in the crystal core, D is the diffusion coefficient (m^2s^{-1}), t is the time (s) and x is the distance from the visually identified interface (m). Eq. (3) rarely gave a satisfactory fit to the whole profile – the regression biases the fit towards the high concentration end, such that the fitted curve overestimates the diffusivity. This is likely due to depletion at the interface, also observed by Chakraborty et al., 1994 and Zhukova et al., 2014 in similar diffusion experiments. To account for this, only the tail end of each profile was fitted. This was done as follows: firstly, the whole profile was fitted to give initial estimates of D, C_{core}, C_{rim}, allowing the characteristic diffusion length scale of $2\sqrt{(Dt)}$ to be calculated. Then, all data points closer to the interface than half of this length scale (cutoff point = $\sqrt{(Dt)}$) were removed, and the residual profile re-fitted. The cut-off position was chosen as a compromise between uncertainties, which increase as the number of data points decrease, and a fit to the tail-end of the profile, which gets better as the cut-off point gets further from the interface.

This method is appropriate for processing the SHRIMP-RG data, where the distance from the interface corresponding to each analysis was directly measured after the analytical session. For the LA-ICP-MS data the situation is slightly more complex – we make the assumption that the long axis of the slit shaped laser beam is exactly perpendicular to the crystal edge (alignment is done manually), and that the decrease of Si counts is associated with the first point at which the laser samples a mix of crystal and resin / buffer. Therefore, we have extra uncertainty relating to the difference between the position of the interface assigned in the ICP-MS data and the actual interface position. We estimate this conservatively as ±10 μm (c.f. the laser

237 width of 6 μm). This was taken into account by adding an interface term (x_0) to (3),
238 fitting the data for x_0 between -10 and +10 μm, then taking the maximum and
239 minimum ±1 s.d. values for the variables D, C_{rim} and C_{core}.

$$C(x,t)=(C_{rim}-C_{core}).\mathrm{erfc}\left(\frac{x-x_0}{\sqrt{4Dt}}\right)+C_{core} \quad (4)$$

240 To account for the depletion at the interface, another analytical solution to Fick's
241 second law was used (Crank, 1975, eq. 3.26, modified for a non-zero core
242 composition), which assumes a constant rate of decrease of ^{26}Mg at the interface:

$$C(x,t)=\left(C_{rim,\,t=0}-C_{core}\right).\left(\mathrm{erfc}\left(\frac{x-x_0}{\sqrt{4Dt}}\right)+4kt\,i^2\mathrm{erfc}\left(\frac{x-x_0}{\sqrt{4Dt}}\right)\right)+C_{core} \quad (5)$$

243 where $i^2\mathrm{erfc}(z)$ is calculated using:

$$i^2\mathrm{erfc}(z)=\frac{1}{4}\left(\mathrm{erfc}(z)-2z\left(\frac{1}{\sqrt{\pi}}e^{-z^2}-z.\mathrm{erfc}(z)\right)\right) \quad (6)$$

244 (Crank, 1975, Table 2.1) and k is a constant describing the rate of decrease/increase of
245 $^{26}Mg/Si$ at the interface (Crank, 1975, eq. 3.25). Again, the $x-x_0$ term in eq. (5) can
246 be replaced by x to remove uncertainty in the position of the assigned interface. The
247 interface concentration of ^{26}Mg (C_{rim}) is assumed to decrease linearly away from its
248 initial state ($C_{rim,\,t=0}$) as a function of time. Changing k leads to a stronger or weaker
249 depletion at the interface, but does not change the length-scale of diffusion, hence the
250 extracted D. This solution gives a good fit to more of the observed diffusion profile
251 than eq. (3), which translates into smaller uncertainties in D. Details of both fitting
252 procedures are shown in Figure 2. Supplementary dataset 1 contains fits to all ^{26}Mg
253 profiles with both methods, along with the processed data.

The two fitting methods – depleting source (eq. (5)) or partial fit to error function (eq. (3)), give Ds within 0.1-0.2 log units, with the partial fit method generally giving slightly lower Ds than the depleting source model (Supplementary Figure 6). However, a total least squares regression of the two sets of Ds to a y=x curve gives χ^2_v = 132, and a y=x+c fit yields c=-0.11 (y=partial fit, x=depleting source), but with χ^2_v = 73, so it is clear that we cannot use the methods interchangeably and extract the same Ds within uncertainty. The extremely high χ^2_v is due to using only the small uncertainties derived from curve fitting. In terms of selecting which method to use herein, both have advantages and drawbacks. The depleting source model is more physically reasonable, but sometimes does not satisfactorily fit all sections of the profiles. It makes the assumption that the decrease at the interface is linear, but this is highly unlikely –conservation of mass in a closed system would predict instead ^{26}Mg versus time relationship that is closer to logarithmic (numerical modelling is presented in Supplementary Figure 7). As a further complication, the system is not closed – there exists a large bed of fo-prEn or fo-per powder below the crystal that should be able to isotopically exchange with the ^{26}Mg-doped source via diffusion along the crystal surface. The partial fit method is good in that it does not make assumptions about the nature of the profile, but effectively just fits its length-scale. The main drawback is the large uncertainties associated with fitting a relatively small number of data points. Therefore, to avoid definitively choosing one method over the other, each curve was fitted by each method then means and uncertainties were combined.

When the uncertainty on the interface position is applied (the x_0 term in eq. (4) and (5)), the uncertainties (calculated as described above) derived from this treatment naturally increase as profiles get shorter (Supplementary Figure 8).

279

280 ## Results

281 **SHRIMP-RG forward versus backwards profiling**

282 A profile measured both forwards (away from the interface) and backwards (towards
283 the interface) are shown in Figure 3a, showing good agreement. This suggests that the
284 SHRIMP-RG is capable of quantifying precisely such short profiles despite
285 considerable spot overlap, albeit for samples where the isotopic enrichment is
286 extreme.

287

288 **LA-ICP-MS vs SHRIMP-RG**

289 Figure 3 shows ^{26}Mg profiles from the experiment successfully measured by both
290 SHRIMP-RG and LA-ICP-MS. For consistency with the LA-ICP-MS data, the
291 SHRIMP-RG data were not normalised to ∑Mg. The concentrations in the crystal
292 cores are in agreement – this is due to the normalisation method used, but the rims are
293 not. Importantly, the diffusion coefficients from the fits fall within uncertainty (1 s.d.
294 shown in the figure) of one another.

295

296 **Mg diffusion**

297 Following the methodology laid out above, extracted diffusion coefficients and their
298 relevant experimental conditions are presented in Table 1. Example profiles are
299 presented in Figure 4.

300

The effect of $aSiO_2$

Diffusivity is consistently higher, by around one order of magnitude, in experiments buffered by Mg_2SiO_4-$Mg_2Si_2O_6$ (high $aSiO_2$) than in those buffered by Mg_2SiO_4-MgO (low $aSiO_2$) at otherwise identical conditions.

The effect of crystal orientation

Mg diffusion is anisotropic, with $D_{[001]}>D_{[010]}>D_{[100]}$. The difference is around 0.5 log units between $D_{[001]}$ and $D_{[010]}$, and between $D_{[010]}$ and $D_{[100]}$, that is, a total of around one order of magnitude difference in diffusion coefficients. This is consistent with anisotropy of diffusion of M-site vacancies in pure forsterite (Demouchy and Mackwell, 2003; Jollands et al., 2016), and diffusion of other divalent M-site cations (e.g. Spandler and O'Neill 2010).

The effect of fO_2

There is no discernible effect of fO_2 on Mg diffusion in pure forsterite, over ~12 orders of magnitude fO_2. This is consistent with the previous experiments in the same system of Chakraborty et al., (1994), which also used forsterite of high purity (11 ppm Fe, approximately similar to ours), and contrasts with the positive fO_2-D relationship from that same study where less pure forsterite was used (120-180 ppm Fe). We note, however, that these Fe values are those of the starting material and do not account for any potential Fe enrichment or depletion occurring during the diffusion experiments.

Fitting to the Arrhenius relationship

Diffusion coefficients as a function of temperature for each $aSiO_2$-orientation condition were fitted individually to the general Arrhenius relationship:

$$\log_{10}D=\log_{10}D_0+\frac{-E_a}{2.303RT} \quad (7)$$

where $\log_{10}D_0$ is the logarithm of the diffusion coefficient (m^2s^{-1}) at 1/T=0 (T=∞), E_a is the activation energy for diffusion in $kJmol^{-1}$, R is the gas constant ($kJmol^{-1}$) and T is the temperature (K). Values of E_a and $\log D_0$ for each axis-buffer pair are presented in Table 2.

An adequate fit of the Ds to eq. (7), as judged from the reduced chi-square of the regression, is not obtained if the uncertainties in $\log_{10}D$ are taken simply as those listed in Table 1, which are from fitting the profiles alone. These uncertainties do not include contributions from (1) uncertainties in temperature; (2) relative uncertainties (between experiments) in the position of the crystal interface; (3) deviations from the assumed constant rate of decrease of ^{26}Mg at the interface (4) non-oblique (to interface) mounting and polishing during post-experiment sample preparation; (5) non-oblique profile measurements and (6) deviations from the principal crystallographic planes..

To obtain a realistic estimate of the total uncertainty, the best fits to eq. (7) were recalculated assuming uncertainties of logD ±0.1 and ±0.2 (1 s.d.), or as observed, whichever was larger. The resulting values of χ^2_v are given in Table 2, for six series of data (three orientations times two $aSiO_2$ values). Realistic uncertainties, incorporating all experimental, analytical and sample-preparation based issues thus appear to fall within the 0.1-0.2 ±logD range.

A global fit

Ea values estimated from Arrhenius plots are between 250-400 kJ mol^{-1}, except for diffusion in enstatite buffered conditions along the a and b axes, for which the temperature range is quite limited. Whilst these activation energies are quite varied,

visual inspection of the trends in Figure 5 suggests that a global fit to eq. (7) may be reasonable, where Q is fixed and $\log D_0$ changes for each $a SiO_2$-orientation condition. This assumes the 1/T versus logD relationships are parallel, based on previous work in similar systems (e.g. Dohmen and Chakraborty, 2007; Zhukova et al., 2014). Thus, all data were fitted by weighted least-squares regression to the equation:

$$\log_{10} D = \log_{10} D_0(a,b,c) + \frac{-Ea}{2.303RT} + m \log a_{SiO_2} \quad (8)$$

This equation contains five parameters to be determined, namely Ea, m, and the three values of Do for each crystallographic orientation, D_0[001], D_0[010], D_0[100]. Values of $aSiO_2$ for the fo-prEn and fo-per buffers were determined from the free energies of the reactions $Mg_2Si_2O_6 = Mg_2SiO_4 + SiO_2$ and $Mg_2SiO_4 = 2MgO + SiO_2$, respectively, using the data from Holland and Powell (2011). The silica activity for each buffer as a function of temperature is shown in Figure 6. Two data (MFO3, periclase-buffered, parallel to [010], MFO9, enstatite-buffered, parallel to [010]) were found to be unusually aberrant (calculated value > 5 s.d. from observed) and were eliminated from the fitting, leaving 47 data. In both cases, there may have been an orientation mix-up – the Ds |||[010] are extremely similar to those |||[001]. Again, the uncertainties as defined in Table 1 give unreasonably high χ^2_v, so these were adjusted as to ±0.15 m^2s^{-1}, or as observed, if the latter was higher. The best fit gave Ea = 298 ± 19 $kJmol^{-1}$, m = 0.59 ± 0.04 and $\log D_0$ parallel to [001] = -5.01 ± 0.02 ; [010] = -5.50 ± 0.02; and [100]: -5.90 ± 0.05 m^2s^{-1}. The reduced chi-square (χ^2_v) for the assumed weighting was 1.1. The uncertainties on the three values of $\log_{10} D_0$ were calculated in two stages, to mitigate the effects of covariance between the parameters, which are large. Firstly, the global best fit was obtained, secondly the fitting was repeated for the three orientations separately, constraining Ea and m at the global best-fit values. These three uncertainties therefore do not include the contribution from their covariances

with Ea and m. We therefore emphasise that the *differences* in the three values of D_0 are very well resolved. A comparison between the final model and the data is given in Figure 7. The value of m is close to that found by Zhukova et al. (2014) for Ni (m = 0.58 ± 0.03), although their value of m for Co was higher (0.80 ± 0.03). Note that these values are switched relative to those given by Zhukova et al. (2014) in their eqs. (9) and (10) due to a mix-up – the Ea and n_{SiO2} given in their Eq. 10 are meant for their Eq. 9, and vice versa. This does not affect the fit parameters (D_0, Ea, n_{SiO2}) from their combined fit (their Eq. 11).

To test our assumption that Ea is constant, independent of crystal orientation, we repeated the fitting allowing Ea to vary with orientation as well as D_0 (7 parameters). However, no improvement in the fit was observed.

Discussion

Comparison with previous studies

Mg diffusion in forsterite has been the subject of several decades of study. Diffusion coefficients from published studies are presented in Figure 8, as a function of temperature. Hallwig et al. (1979), Sockel and Hallwig (1977) and Sockel et al. (1980) measured experimental ^{26}Mg profiles using SIMS depth profiling. They used a thin film of Mg_2SiO_4 composition enriched in ^{26}Mg as the diffusant source, hence $aSiO_2$ was unconstrained. Morioka (1981) conducted three experiments at 1300-1400 °C by evaporating, from solution, ^{26}MgO onto the surface of a crystal and then placing the crystal – film couples into quartz crucibles for annealing. The use of quartz crucibles may have buffered the experiment at high $aSiO_2$, i.e. corresponding to the Mg_2SiO_4 – $Mg_2Si_2O_6$ equilibrium. Andersson (1987) (PhD Thesis, then published as Andersson and Borchardt (1989) and Andersson et al. (1989)) used

NPB-SIMS (Neutral Primary Beam SIMS) depth profiling to measure D_{Si}, D_O and D_{Mg} simultaneously, in fully aSiO$_2$-buffered experiments between 1100-1450 °C. Whilst diffusive anisotropy is reported (Andersson et al., 1989), with $D_c>D_b>D_a$, the raw data (Andersson, 1987) do not support this well – the data show over one order of magnitude discrepancy between replicate experiments and time series steps. The sensitivity of the then newly developing analytical technique was likely insufficient to distinguish these order-of-magnitude variations, although they did successfully demonstrate that $D_{Si}<<D_{Mg}$. Chakraborty et al. (1994) revisited the problem, studying the two different forsterite crystals, one with very low Fe (<10 ppm), the other with >100 ppm Fe, and fO$_2$ and aSiO$_2$. They found no aSiO$_2$ dependence within the sensitivity of their analytical technique, hence conducted most experiments in aSiO$_2$-unbuffered conditions. An fO$_2$ dependence was observed in the less pure forsterite (probably due to Fe^{3+}-associated M-site vacancies), whereas no dependence was seen in the very pure forsterite, in line with this study. Fei et al. (2018) extended the dataset to higher pressures (up to 13 GPa) using polycrystalline forsterite aggregates rather than single crystals, and also considered the effect of fH$_2$O on D_{Mg}. They found D_{Mg} broadly in agreement with previous data, but also showed a pressure effect (ΔV=4.3 cm^3/mol^{-1}), and that D_{Mg} is positively dependent on fH$_2$O. Whilst outside the scope of this work, it is curious to note that this D_{Mg}-fH$_2$O dependence exists despite the infrared spectra of their experimental olivine showing no O-H stretching bands associated with hydrogen on the M-sites, only H associated with T-site vacancies (e.g. Lemaire et al., 2004; Matveev et al., 2001; Tollan et al., 2017).

Despite both Chakraborty et al. (1994) and Andersson (1987) conducting experiments with explicit aSiO$_2$ buffering, no aSiO$_2$ dependence was found. The results from Andersson (1987) showed scatter so considerable (Figure 8) that this is not surprising

– the ~1 order of magnitude effect of $a\mathrm{SiO_2}$ would not be resolvable. The reason Chakraborty et al. (1994) saw no effect is less obvious. Their replicate measurements on the same sample differ by up to ~0.3 log units, but this is still smaller than the effect of $a\mathrm{SiO_2}$ found in this study.

An insight is provided by our experiences in this study. In several preliminary experiments, we found that buffering $a\mathrm{SiO_2}$ under the constraints of economizing on high-cost materials like isotopically enriched sources can be troublesome, if there are multiple parts of the experimental charge attempting to impose different $a\mathrm{SiO_2}$ on the crystal. In these problematic experiments, all crystals were placed onto a bed of nominally pure forsterite powder, synthesised from MgO and $\mathrm{SiO_2}$. However, because the nominally pure forsterite most likely has some deviation from perfect (2:1) Mg:Si stoichiometry, it will have an intrinsic, if unknown, capacity to buffer the $a\mathrm{SiO_2}$. In previous experimental campaigns by our group studying chemical, not tracer diffusion (Zhukova et al., 2014, 2017, 2018, Jollands et al., 2014, 2018) we did not encounter this problem because we were able to use large amounts of inexpensive buffering powder for each experiment. In the present study, we initially used the minimum possible volume of ^{26}Mg-doped powder for each experiment, which apparently led to the buffering capacity of the powder glued onto the crystal surface being overwhelmed by that of the powder bed, thus several of these early experiments gave identical results for the fo-per and fo-prEn buffered runs. When the experimental design was modified, making use of a forsterite-enstatite or periclase bed, the differences between the buffering conditions systematically appeared.

This may have been the case in the Chakraborty et al. (1994) experiments, where the ^{26}Mg source was a MgO film (low $a\mathrm{SiO_2}$), and then the crystal-film couples were surrounded by MgO or $\mathrm{Mg_2Si_2O_6}$ powder, or nothing. Potentially, the MgO film was

able to buffer the near-surface region (i.e. at least the top micrometres) of the crystals to low $a\mathrm{SiO_2}$, even if $\mathrm{Mg_2Si_2O_6}$ was present nearby. If their $\mathrm{Mg_2Si_2O_6}$ powder was acting as a true buffer, the MgO film should have fully reacted to $\mathrm{Mg_2SiO_4}$ – it is not clear whether this occurred.

In any case, our data show, for the first time, that D_{Mg} is a function of $a\mathrm{SiO_2}$, as would be expected from general considerations of the effect of $a\mathrm{SiO_2}$ on M-site vacancy concentration in forsterite (e.g. Plushkell and Engell, 1968; Smyth and Stocker, 1975; Stocker and Smyth, 1978). We may suggest that the Morioka (1981) experiments were unintentionally conducted at high $a\mathrm{SiO_2}$ (quartz crucibles) and the Chakraborty et al. (1994) experiments at low $a\mathrm{SiO_2}$ (MgO film), and even that the Sockel and Hallwig (1977) experiments were at high $a\mathrm{SiO_2}$ due to Si-enrichment during film deposition, if this process produced effects similar to those of pulsed laser deposition (Dohmen et al., 2002a). This would explain the sequence of results in which $D_{Mg}(\text{Morioka}) \approx D_{Mg}(\text{Sockel,Hallwig}) > D_{Mg}(\text{Chakraborty})$, and why the Chakraborty et al. (1994) data agree, when extrapolated in temperature, with our low $a\mathrm{SiO_2}$ series (Figure 9), and the Morioka (1981) experiments agree with our fo-prEn buffered data. An enlarged comparison of our data and that of Chakraborty et al. (1994) and Morioka (1981) is shown in Figure 9. If our interpretation is correct, then an extended global fit, incorporating their data, is possible. Utilising the results of Chakraborty et al. (1994) considerably extends the range of temperature covered, resulting in improved accuracy of the activation energy (Ea) from the global fit, giving:

$Ea = 359 \pm 10\ \mathrm{kJmol^{-1}}$,

$m = 0.61 \pm 0.03\ \mathrm{m^2 s^{-1}}$

$\log D_0$ |||[001] = -3.15 ± 0.08; |||[010] = -3.61 ± 0.02; |||[100]: -4.01 ± 0.05 $\mathrm{m^2 s^{-1}}$.

472

473 **Point defects and charge neutrality conditions**

474 The global best fit, including previously published data, gave m = 0.61 ± 0.03, that is,
475 $D^*_{Mg} \propto a^{0.61}_{SiO_2}$, similar to that found for Ni chemical diffusion by Zhukova et al. (2014).
476 Assuming that the diffusivity of Mg is proportional to the concentration of M-site
477 vacancies, it allows a relationship between externally imposed chemical activities and
478 the population of point defects in the crystal to be described.
479 The relationship between the concentration of M-site vacancies and $aSiO_2$ in pure, Fe-
480 free forsterite has been proposed to be related either to the concentration of interstitial
481 Si^{4+}, $\{Si_i^{\bullet\bullet\bullet\bullet}\text{-}2V_M^{''}\}^{\times}$, or to O vacancies $\{V_O^{\bullet\bullet}\text{-}V_M^{''}\}^{\times}$ (Smyth and Stocker, 1975; Stocker
482 and Smyth, 1978). In the first case, $[V_M^{''}] \propto aSiO_2^{2/3}$, and in the latter, $[V_M^{''}] \propto$
483 $aSiO_2^{1/4}$, with no relationship between $[V_M^{''}]$ and fO_2 in either case. While the present
484 results are closer to the former, the best-fit exponent is resolvably lower than 2/3. A
485 possible explanation may be that M-site vacancies are produced by both mechanisms.
486 This assertion could be independently tested by determining the tracer diffusivity of O
487 in pure forsterite as a function of $aSiO_2$ at constant fO_2: the creation of O vacancies
488 implies $D_O^* \propto a_{SiO_2}^{1/4}$, whereas if $D_O^* \propto a_{SiO_2}^0$ (no relationship) at constant fO_2, this would
489 support the apparently favoured $[V_{Mg}^{''}]=2[Si_i^{\bullet\bullet\bullet\bullet}]$ charge neutrality condition (Smyth
490 and Stocker, 1975; Stocker and Smyth, 1978).
491 It might also be the case that trace elements control the defect population to some
492 extent, as recently demonstrated using forsterite from the same supply (Le Losq et al.,
493 2019). The fO_2 independence of ^{26}Mg diffusion suggests Fe is not a likely candidate
494 for controlling Mg diffusion in these experiments. Al (present at the level of several
495 tens of wt. ppm in our crystals) could be a potential candidate, especially given its
496 ability to reside on both the tetrahedral and octahedral sites in forsterite. For example,

497 a reaction that enables Al to move from the tetrahedral site to the octahedral site,
498 forming M-site vacancies ([vac]), in the presence of enstatite can be written:

$$\underset{\text{ol}}{2MgAl_2O_4}+\underset{\text{opx}}{4Mg_2Si_2O_6}=3\underset{\text{ol}}{\left(Al_{\frac{4}{3}}[vac]_{\frac{2}{3}}\right)SiO_4}+\underset{\text{ol}}{5Mg_2SiO_4} \quad (9)$$

499 However, this reaction is formulated for the crystal-buffer interface. Similar reactions
500 rearranging Al from the tetrahedral to octahedral site within the crystal, where site
501 balance has to be maintained, are much more complex and would likely have to
502 involve other point defects. For example, (10) is an interaction between the Al
503 Tschermak's type defect and an interstitial Si^{4+} charged-balanced by two M-site
504 vacancies (presented in Kröger-Vink notation):

$$\{Al_T^{'}\text{-}Al_M^{\bullet}\}^{\times}+\{Si_i^{\bullet\bullet\bullet\bullet}\text{-}2V_M^{''}\}^{\times}=\{2Al_M^{\bullet}\text{-}V_M^{''}\}^{\times}+Si_{Si}^{\times} \quad (10)$$

505 Thus, in order for Al to control the defect population within the crystal by
506 rearrangement, there must either be some complex interaction with other defects, or
507 Al diffusion must be fast enough to modify the M-site vacancy population via
508 diffusion of the $\{2Al_M^{\bullet}\text{-}V_M^{''}\}^{\times}$ association. The latter could be possible- the fast
509 mechanism for Al diffusivity in forsterite (Zhukova et al., 2017) is at least two orders
510 of magnitude higher than that of Mg (this study). In terms of concentrations, 30 wt.
511 ppm of Al in $\{2Al_M^{\bullet}\text{-}V_M^{''}\}^{\times}$ configuration, in pure forsterite, is equivalent to around
512 $1.6\text{x}10^{-4}$ apfu Al, i.e. $[V_M^{''}]\approx 8\text{x}10^{-5}$, which is in the same order of magnitude as $[V_M^{''}]$
513 associated with Fe^{3+} in Fe-bearing olivine (Dohmen and Chakraborty, 2007), which is
514 well known to affect Fe-Mg inter-diffusion. Thus, even ten, or tens of wt. ppm Al
515 could considerably alter the point defect population of pure forsterite, which will have
516 a lower background vacancy population than Fe-bearing olivine.
517

518 **The effect of $aSiO_2$ on diffusion of different cations in forsterite**

519 Following several similar experimental campaigns where different trace/minor
520 elements have been diffused into forsterite/olivine at fully buffered aSiO$_2$ conditions,
521 some observations can be compiled. One first order observation is that the effect of
522 $aSiO_2$ is not equal for all trace elements. The largest effects of $aSiO_2$ (>2 orders
523 magnitude) on D were observed for Al^{3+} (Zhukova et al., 2017) although some of this
524 effect may be due to higher diffusant concentration in high aSiO$_2$ experiments, and
525 concentration-dependent diffusion. The smallest effects (approximately no effect)
526 were observed for Ca^{2+} (Bloch et al., 2019). The notable difference between these
527 cations is their octahedrally-coordinated ionic radii (Al^{3+}:0.54; Cr^{3+}:0.62; Ca^{2+}:1),
528 where the larger cations are preferentially ordered into the M2 site, and smaller
529 cations the M1 (although ionic radius is not the only parameter controlling site
530 preference-crystal field effects (e.g. Burns, 1970) and covalent bond strength (e.g.
531 (Ghose and Wan, 1974) are also important).
532 The link between M-site preference and effect of aSiO$_2$ on diffusivity could be
533 explained by the M1 preference of M-site vacancies (Brodholt, 1997; Walker et al.,
534 2009). Large M2 site cations are less likely to encounter M-site vacancies than
535 smaller M1-site cations. Therefore, M2 site cations may be relatively immune to
536 external variations in aSiO$_2$, whereas M1 cations would be readily affected.

537 Figure 10 shows the difference between logD at high aSiO$_2$ and at low aSiO$_2$ for a
538 series of cations, firstly against ionic radii, then qualitatively against likely site
539 preference. Where available, references describing site preference are given in the
540 caption. Figure 10 suggests that there is some relationship between the effect of aSiO$_2$
541 on D and M site preference. However, the inability to place a quantitative constraint

on site preference, and (possibly) hence the data scatter, makes describing this important relationship in any physical sense premature at this time.

This relationship could be explored further by considering the effect of $a\mathrm{SiO_2}$ on diffusive anisotropy in a simple system with diffusants showing M1 site preference (e.g. Ni, Co in forsterite) where no complications from concentration-dependent diffusion exist (Zhukova et al. (2014) only considered Ni and Co diffusion parallel to [100] in forsterite). Given that the M1 sites form chains parallel to [001], it may be that the response of D to $a\mathrm{SiO_2}$ is greater parallel to [001] than [010] or [100]. This would also depend, for example, on the extent to which macroscopically measurable diffusion parallel to [001] is the sum of diffusive hops occurring only ~||[001] – such experiments would help shed light on this question as well. Alternatively, the effect of $a\mathrm{SiO_2}$ on the diffusion of the trivalent cations could be studied systematically – it may be expected that La (1.03 Å) is less sensitive to $a\mathrm{SiO_2}$ than Lu (0.89 Å) or Sc (0.75 Å).

Implications

Mg diffusion in forsterite, like many other cations, is a function of silica activity, along with temperature, pressure, crystallographic orientation, and water fugacity (Chakraborty et al., 1994; Fei et al., 2018). This dependence will propagate forwards into any geochemical transport behaviour that depends on Mg diffusion. Apparent discrepancies between diffusion studies may potentially be explained by differences in the buffering of major element chemical potentials, as in this study, or could alternatively be related to differences in impurities such as Al and Fe that can have a large influence on the number and positions of point defects.

Regarding the usefulness of various cations for diffusion chronometry, not all cations can be considered equal. The best should be those where diffusivity is a function of temperature, but little else. The safest element in olivine is probably calcium, which is unaffected by silica activity (Bloch et al., 2019), is approximately isotropic (Coogan et al., 2005), often shows simple diffusion profiles (Qian et al., 2010), and is generally easy to measure in natural systems (De Hoog et al., 2010). To be truly useful, Ca diffusion must also be unaffected by the fugacity of water in the system – this remains to be explored. However, we note that most applications of olivine diffusion chronometry have been done on olivine crystals in systems where the activity of silica is high enough (e.g. in basalt, kimberlite, dolerite etc) that an olivine-pyroxene simple system is a good approximation.

Looking forwards, for systems where the chemical activities are unknown, there exists the tantalising possibility that relative profile length scales could be used as activity monitors.

Acknowledgements

Trevor Ireland, Peter Holden, Morgan Williams, Laure Gauthiez-Putallaz and Mari-Rosa Schiccitano are thanked for help with various aspects of SHRIMP analyses. Joshua Muir, Andrew Walker, Othmar Müntener, Elias Bloch, Jung-Woo Park, Carl Mitchell, Dave Clark and Dean Scott are acknowledged for various assistance and useful discussions. Daniele Cherniak and an anonymous reviewer are thanked for reviews that helped to strengthen the manuscript.

References

590 Andersen, O. and Bowen, N. (1914) Das binäre System Magnesiumoxyd-Silicium-2-
591 oxyd. Zeitschrift für anorganische Chemie 87, 283-299.
592 Andersson, K. (1987) Materietransport und Defektstrukturen in kristallinem
593 Magnesiumorthosilicat bei höheren Temperaturen. PhD Thesis, Technischen
594 Universität Clausthal.
595 Andersson, K. and Borchardt, G. (1989) Defect structure and self diffusion in
596 Mg_2SiO_4 (forsterite) at high temperature, Non-Stoichiometric Compounds. Springer,
597 pp. 399-409.
598 Andersson, K., Borchardt, G., Scherrer, S., Weber, S., 1989. Self-diffusion in
599 Mg_2SiO_4 (forsterite) at high temperature. Fresenius Zeitschrift für analytische Chemie
600 333, 383-385.
601 Ando, K., Kurokawa, H., Oishi, Y., Takei, H., 1981. Self-Diffusion Coefficient of
602 Oxygen in Single-Crystal Forsterite. Communications of the American Ceramic
603 Society 64, C30.
604 Bejina, F., Jaoul, O., Liebermann, R.C., 1999. Activation volume of Si diffusion in
605 San Carlos olivine: Implications for upper mantle rheology. Journal of Geophysical
606 Research-Solid Earth 104, 25529-25542.
607 Bloch, E.M., Jollands, M.C., Gerstl, S.S.A., Bouvier, A.S., Plane, F., Baumgartner,
608 L.P. (2019) Diffusion of calcium in forsterite and ultra-high resolution of
609 experimental diffusion profiles in minerals using local electrode atom probe
610 tomography. Geochimica et Cosmochimica Acta.
611 Brodholt, J. (1997) Ab initio calculations on point defects in forsterite (Mg_2SiO_4) and
612 implications for diffusion and creep. American Mineralogist 82, 1049-1053.
613 Buening, D.K. and Buseck, P.R. (1973) Fe-Mg Lattice Diffusion in Olivine. Journal
614 of Geophysical Research 78, 6852-6862.

615 Burns, R.G. (1970) Site preferences of transition metal ions in silicate crystal
616 structures. Chemical Geology 5, 275-283.
617 Chakraborty, S., 1997. Rates and mechanisms of Fe-Mg interdiffusion in olivine at
618 980-1300°C. Journal of Geophysical Research-Solid Earth 102, 12317-12331.
619 Chakraborty, S., Farver, J.R., Yund, R.A., Rubie, D.C., 1994. Mg Tracer Diffusion in
620 Synthetic Forsterite and San-Carlos Olivine as a Function of P, T and fO_2. Physics
621 and Chemistry of Minerals 21, 489-500.
622 Cherniak, D. J., and Watson, E. B., 2012, Diffusion of helium in olivine at 1 atm and
623 2.7 GPa: Geochimica Et Cosmochimica Acta, v. 84, p. 269-279.
624 Cherniak, D.J. and Liang, Y. (2014) Titanium diffusion in olivine. Geochimica Et
625 Cosmochimica Acta 147, 43-57.
626 Cherniak, D.J., 2010. REE diffusion in olivine. American Mineralogist 95, 362-368.
627 Coogan, L.A., Hain, A., Stahl, S., Chakraborty, S., 2005. Experimental determination
628 of the diffusion coefficient for calcium in olivine between 900°C and 1500°C.
629 Geochimica et Cosmochimica Acta 69, 3683-3694.
630 Costa, F., Chakraborty, S., 2008. The effect of water on Si and O diffusion rates in
631 olivine and implications for transport properties and processes in the upper mantle.
632 Physics of the Earth and Planetary Interiors 166, 11-29.
633 Crank, J., 1975. The Mathematics of Diffusion. Oxford University Press, Oxford.
634 Crépisson, C., O'Neill, H.S.C., Hermann, J. and Spandler, C. (2012) Diffusion of
635 Yttrium in olivine, European Mineralogical Conference.
636 De Hoog, J. C., Gall, L., and Cornell, D. H., 2010, Trace-element geochemistry of
637 mantle olivine and application to mantle petrogenesis and geothermobarometry:
638 Chemical Geology, v. 270, no. 1, p. 196-215.

639 Demouchy, S. and Mackwell, S. (2003) Water diffusion in synthetic iron-free
640 forsterite. Physics and Chemistry of Minerals 30, 486-494.
641 Demouchy, S. and Mackwell, S. (2006) Mechanisms of hydrogen incorporation and
642 diffusion in iron-bearing olivine. Phys Chem Miner 33.
643 Dohmen, R., Becker, H.W., Chakraborty, S., 2007. Fe-Mg diffusion in olivine I:
644 experimental determination between 700 and 1,200°C as a function of composition,
645 crystal orientation and oxygen fugacity. Physics and Chemistry of Minerals 34, 389-
646 407.
647 Dohmen, R., Becker, H.W., Meissner, E., Etzel, T. and Chakraborty, S. (2002a)
648 Production of silicate thin films using pulsed laser deposition (PLD) and applications
649 to studies in mineral kinetics. European Journal of Mineralogy 14, 1155-1168.
650 Dohmen, R., Chakraborty, S., 2007. Fe-Mg diffusion in olivine II: point defect
651 chemistry, change of diffusion mechanisms and a model for calculation of diffusion
652 coefficients in natural olivine. Physics and Chemistry of Minerals 34, 597-598.
653 Dohmen, R., Chakraborty, S., Becker, H.-W., 2002b. Si and O diffusion in olivine
654 and implications for characterizing plastic flow in the mantle. Geophysical Research
655 Letters 29, 2030.
656 Fei, H., Koizumi, S., Sakamoto, N., Hashiguchi, M., Yurimoto, H., Marquardt, K.,
657 Miyajima, N. and Katsura, T. (2018) Mg lattice diffusion in iron-free olivine and
658 implications to conductivity anomaly in the oceanic asthenosphere. Earth and
659 Planetary Science Letters 484, 204-212.
660 Fei, H., Wiedenbeck, M., Yamazaki, D. and Katsura, T. (2013) Small effect of water
661 on upper-mantle rheology based on silicon self-diffusion coefficients. Nature 498,
662 213-215.

663 Fei, H.Z., Hegoda, C., Yamazaki, D., Wiedenbeck, M., Yurimoto, H., Shcheka, S.,
664 Katsura, T., 2012. High silicon self-diffusion coefficient in dry forsterite. Earth and
665 Planetary Science Letters 345, 95-103.
666 Ghose, S. and Wan, C.n. (1974) Strong site preference of Co^{2+} in olivine,
667 $Co_{1.10}Mg_{0.90}SiO_4$. Contributions to Mineralogy and Petrology 47, 131-140.
668 Hallwig, D., Schachtner, R., Sockel, H., 1979. Diffusion of magnesium, silicon and
669 oxygen in Mg_2SiO_4 and formation of the compound in the solid state, Proceedings of
670 the 10th International Conference 'Science of Ceramics'. Berchtesgaden, W.
671 Germany, 1979. Ed: H. Hausner.
672 Hier-Majumder, S., Anderson, I.M. and Kohlstedt, D.L. (2005) Influence of protons
673 on Fe-Mg interdiffusion in olivine. Journal of Geophysical Research-Solid Earth 110.
674 Holland, T. and Powell, R. (2011) An improved and extended internally consistent
675 thermodynamic dataset for phases of petrological interest, involving a new equation
676 of state for solids. Journal of Metamorphic Geology 29, 333-383.
677 Ito, M. and Ganguly, J. (2006) Diffusion kinetics of Cr in olivine and ^{53}Mn–^{53}Cr
678 thermochronology of early solar system objects. Geochimica et Cosmochimica Acta
679 70, 799-809.
680 Jaoul, O., Froidevaux, C., Durham, W.B., Michaut, M., 1980. Oxygen Self-Diffusion
681 in Forsterite - Implications for the High-Temperature Creep Mechanism. Earth and
682 Planetary Science Letters 47, 391-397.
683 Jochum, K.P., Weis, U., Stoll, B., Kuzmin, D., Yang, Q., Raczek, I., Jacob, D.E.,
684 Stracke, A., Birbaum, K., Frick, D.A., Günther, D. and Enzweiler, J. (2011)
685 Determination of Reference Values for NIST SRM 610–617 Glasses Following ISO
686 Guidelines. Geostandards and Geoanalytical Research 35, 397-429.

687 Jollands, M., O'Neill, H.S.C., Van Orman, J., Berry, A., Hermann, J., Newville, M.
688 and Lanzirotti, A. (2018) Substitution and diffusion of Cr^{2+} and Cr^{3+} in synthetic
689 forsterite and natural olivine at 1200–1500° C and 1 bar. Geochimica et
690 cosmochimica acta 220, 407-428.
691 Jollands, M.C., Hermann, J., O'Neill, H.S.C., Spandler, C. and Padrón-Navarta, J.A.
692 (2016a) Diffusion of Ti and some Divalent Cations in Olivine as a Function of
693 Temperature, Oxygen Fugacity, Chemical Potentials and Crystal Orientation. Journal
694 of Petrology 57, 1983-2010.
695 Jollands, M.C., O'Neill, H.St.C., Hermann, J., 2014. The importance of defining
696 chemical potentials, substitution mechanisms and solubility in trace element diffusion
697 studies: the case of Zr and Hf in olivine. Contributions to Mineralogy and Petrology
698 168, 1-19.
699 Jollands, M.C., Padrón-Navarta, J.A., Hermann, J. and O'Neill, H.S.C. (2016b)
700 Hydrogen diffusion in Ti-doped forsterite and the preservation of metastable point
701 defects. American Mineralogist 101, 1560-1570.
702 Jurewicz, A.J.G. and Watson, E.B. (1988) Cations in Olivine .1. Calcium Partitioning
703 and Calcium-Magnesium Distribution between Olivines and Coexisting Melts, with
704 Petrologic Applications. Contributions to Mineralogy and Petrology 99, 176-185.
705 Le Losq, C., Jollands, M. C., Tollan, P. M. E., Hawkins, R., and O'Neill, H. S. C.,
706 2019, Point defect populations of forsterite revealed by two-stage metastable
707 hydroxylation experiments: Contributions to Mineralogy and Petrology, 174, 53.
708 Lemaire, C., Kohn, S. and Brooker, R. (2004) The effect of silica activity on the
709 incorporation mechanisms of water in synthetic forsterite: a polarised infrared
710 spectroscopic study. Contributions to Mineralogy and Petrology 147, 48-57.

Li, J.-P., O'Neill, H.S.C. and Seifert, F. (1995) Subsolidus Phase Relations in the System MgO-SiO_2-Cr-O in Equilibrium with Metallic Cr, and their Significance for the Petrochemistry of Chromium. Journal of Petrology 36, 107-132.

Longerich, H., Jackson, S., and Gunther, D., 1996, Laser ablation inductively coupled plasma mass spectrometric transient signal data acquisition and analyte concentration calculation. Journal of Analytical Atomic Spectroscopy 11, 899-904.

Lumpkin, G.R., Ribbe, P.H. and Lumpkin, N.E. (1983) Composition, order-disorder and lattice parameters of olivines; determinative methods for Mg-Mn and Mg-Ca silicate olivines. American Mineralogist 68, 1174-1182.

Matsui, Y. and Syono, Y. (1968) Unit cell dimensions of some synthetic olivine group solid solutions. Geochemical Journal 2, 51-59.

Matveev, S., O'Neill, H.S.C., Ballhaus, C., Taylor, W.R. and Green, D. (2001) Effect of silica activity on OH− IR spectra of olivine: implications for low-aSiO2 mantle metasomatism. Journal of Petrology 42, 721-729.

Morioka, M., 1981. Cation Diffusion in Olivine .2. Ni-Mg, Mn-Mg, Mg and Ca. Geochimica et Cosmochimica Acta 45, 1573-1580.

Mukhopadhyay, D.K. and Lindsley, D.H. (1983) Phase relations in the join kirschsteinite ($CaFeSiO_4$)-fayalite (Fe_2SiO_4). American Mineralogist 6, 1089-1094.

O'Neill, H.S.C. (1987) Quartz-fayalite-iron and quartz-fayalite-magnetite equilibria and the free energy of formation of fayalite (Fe_2SiO4) and magnetite (Fe_3O_4). American Mineralogist 72, 67-75.

Paton, C., Hellstrom, J., Paul, B., Woodhead, J. and Hergt, J. (2011) Iolite: Freeware for the visualisation and processing of mass spectrometric data. Journal of Analytical Atomic Spectrometry 26, 2508-2518.

735 Petričević, V., Gayen, S.K., Alfano, R.R., Yamagishi, K., Anzai, H. and Yamaguchi,
736 Y. (1988) Laser action in chromium - doped forsterite. Appl Phys Lett 52, 1040-
737 1042.
738 Petry, C., Chakraborty, S., Palme, H., 2004. Experimental determination of Ni
739 diffusion coefficients in olivine and their dependence on temperature, composition,
740 oxygen fugacity, and crystallographic orientation. Geochimica et Cosmochimica Acta
741 68, 4179-4188.
742 Plushkell, W., Engell, H.J., 1968. Ionen und Elektronenleitung in Magnesium
743 Orthosilikat. Berichte der Deutschen Keramischen Gesellschaft 45, 388.
744 Qian, Q., O'Neill, H.S.C., Hermann, J., 2010. Comparative diffusion coefficients of
745 major and trace elements in olivine at similar to 950 °C from a xenocryst included in
746 dioritic magma. Geology 38, 331-334.
747 Reddy, K.P.R., Oh, S.M., Major, L.D., Cooper, A.R., 1980. Oxygen Diffusion in
748 Forsterite. Journal of Geophysical Research 85, 322-326.
749 Ryerson, F.J., Durham, W.B., Cherniak, D.J. and Lanford, W.A. (1989) Oxygen
750 Diffusion in Olivine - Effect of Oxygen Fugacity and Implications for Creep. J
751 Geophys Res-Solid 94, 4105-4118.
752 Schindelin, J., Rueden, C.T., Hiner, M.C. and Eliceiri, K.W. (2015) The ImageJ
753 ecosystem: An open platform for biomedical image analysis. Molecular Reproduction
754 and Development 82, 518-529.
755 Smyth, D.M., Stocker, R.L., 1975. Point defects and non-stoichiometry in forsterite.
756 Physics of the Earth and Planetary Interiors 10, 183-192.
757 Sockel, H. and Hallwig, D. (1977) Ermittlung kleiner Diffusionskoeffizienten mittels
758 SIMS in oxydischen Verbindungen, Achtes Kolloquium über Metallkundliche

759 Analyse mit Besonderer Berücksichtigung der Elektronenstrahl-und Ionenstrahl-
760 Mikroanalyse Wien, 27. bis 29. Oktober 1976. Springer, pp. 95-107.
761 Sockel, H.G., Hallwig, D., Schachtner, R., 1980. Investigations of slow exchange
762 processes at metal and oxide surfaces and interfaces using secondary ion mass
763 spectrometry. Materials Science and Engineering 42, 59-64.
764 Spandler, C., O'Neill, H.S.C., 2010. Diffusion and partition coefficients of minor and
765 trace elements in San Carlos olivine at 1,300°C with some geochemical implications.
766 Contributions to Mineralogy and Petrology 159, 791-818.
767 Spandler, C., O'Neill, H.S.C., Kamenetsky, V.S., 2007. Survival times of anomalous
768 melt inclusions from element diffusion in olivine and chromite. Nature 447, 303-306.
769 Stocker, R., Smyth, D., 1978. Effect of enstatite activity and oxygen partial pressure
770 on the point-defect chemistry of olivine. Physics of the Earth and Planetary Interiors
771 16, 145-156.
772 Tollan, P. M. E., Smith, R., O'Neill, H. S. C., and Hermann, J., 2017, The responses
773 of the four main substitution mechanisms of H in olivine to H_2O activity at 1050 °C
774 and 3 GPa: Progress in Earth and Planetary Science, v. 4, no. 1, p. 14.
775 Walker, A.M., Woodley, S.M., Slater, B. and Wright, K. (2009) A computational
776 study of magnesium point defects and diffusion in forsterite. Physics of the Earth and
777 Planetary Interiors 172, 20-27.
778 Wang, Z.Y., Hiraga, T. and Kohlstedt, D.L. (2004) Effect of H+ on Fe-Mg
779 interdiffusion in olivine, $(Fe,Mg)_2SiO_4$. Appl Phys Lett 85, 209-211.
780 Zhukova, I., O'Neill, H., Campbell, I.H., Fiorentini, M., Kilburn, M. and Guagliardo,
781 P. (2018) Diffusion and solubilities of Rh, Ru and Ir in olivine and spinel. Chemical
782 Geology 494, 19-29.

783 Zhukova, I., O'Neill, H. and Campbell, I.H. (2017) A subsidiary fast-diffusing
784 substitution mechanism of Al in forsterite investigated using diffusion experiments
785 under controlled thermodynamic conditions. Contributions to Mineralogy and
786 Petrology 172, 53.
787 Zhukova, I., O'Neill, H.S., Cambell, I.H., Kilburn, M.R., 2014. The effect of silica
788 activity on the diffusion of Ni and Co in olivine. Contributions to Mineralogy and
789 Petrology 168, 1-15.
790

791 **Figure Captions**

792 Figure 1: Backscattered electron images (obtained using an Oxford Instruments
793 CamScan scanning electron microscope (SEM) at the University of Lausanne) of a fo-
794 prEn buffered sample post-experiment and post-analysis, mounted in, and
795 impregnated with epoxy. (a) Wide view, showing the nature of the buffering layer,
796 several laser tracks scanning from core to rim (and into the epoxy) with arrows
797 denoting the direction of laser movement relative to the sample surface, and two
798 single laser shots, used for orientation before analysis. (b) is a closer view of the area
799 in (a) delimited by the white square. Larger versions of the same figure, and other
800 SEM images, can be found in Supplementary Figure 2.

801 Figure 2: Details regarding the fitting procedures for ^{26}Mg, to show the different
802 model geometries from the three methods. The profile is from a 1500 °C, fo-prEn
803 buffered, diffusion ||[001] experiment. (a) Fit of the whole profile to eq. (3). The
804 fitted curve fails to adequately model the whole profile, notably at the tail-end. (b)
805 Partial fit using eq. (3), where all data before the $\sqrt{(Dt)}$ point, from (a), have been
806 removed from fitting. (c) Fit of the full profile to eq. (5), although without the x_0

807 term. The best-fit values of logD using the three methods, associated with the three
808 figures are (a) -13.98 m^2s^{-1}; (b) -14.14 m^2s^{-1} and (c) -14.13 m^2s^{-1}, respectively.

809 Figure 3: (a) comparison between a forward and backward profile measured by
810 SHRIMP-RG, showing within uncertainty agreement (1 s.d. shown). (b) comparison
811 between LA-ICP-MS and SHRIMP-RG data for the 1250 °C, forsterite-periclase
812 buffered (846720 s, air, [001]) experiment successfully measured by both techniques,
813 showing within-uncertainty agreement in diffusivity, but a slight disagreement in
814 concentrations.

815 Figure 4: Some example LA-ICP-MS profiles from this study, including fits to eq.
816 (5). Panels are arranged such that temperature increases from top to bottom, with the
817 two left columns representing diffusion along [001] and the right columns
818 representing diffusion along [100] or [010] (except for the bottom row). For each
819 orientation, profiles are shown for the two buffering conditions, with a profile from
820 the other buffering condition shown in grey (i.e. the greyed profile in (a) is the main
821 profile in (b), etc.). Enstatite-buffered experiments suffered partial melt at >1500°C,
822 so only periclase-buffered experiments are shown in the lowermost row.

823 Figure 5: The effects of chemical activities, crystal orientation, oxygen fugacity and
824 temperature on Mg diffusion. (a) Diffusion along [001] for experiments buffered
825 either by fo-per or fo-prEn. Despite the scatter, there is a clear difference of around
826 one order of magnitude between the datasets. (b) fo-per buffered experiments for
827 diffusion along the [001], [010] and [100] directions. Diffusion is fastest along [001]
828 and slowest along [100]. (c) No apparent effect of oxygen fugacity on diffusion in
829 either buffering condition.

Figure 6: Silica activity ($a\mathrm{SiO_2}$) as a function of inverse temperature. Grey areas: ranges of experimental conditions. The liquidus of fo-prEn is from Andersen and Bowen (1914).

Figure 7: Comparison of measured versus model diffusion coefficients, including a 1:1 line and 1:1±0.25 logD lines.

Figure 8: Diffusion coefficients from previous published studies of ^{26}Mg diffusion in forsterite, and //[001] diffusion coefficients from this study, with conditions described in the text. Abbreviations: C94: Chakraborty et al. (1994); S80: Sockel et al. (1980); M81: Morioka et al. (1981), A87: Andersson (1987); F18: Fei et al. (2018).

Figure 9: Data from this study (diffusion //[001]), along with the data from Morioka (1981) and Chakraborty et al. (2004). (a) shows the best fits to all data. Dashed lines represent the best fits to only the dataset from this study. Solid lines also include the data from Chakraborty et al. (1994) and Morioka (1981), assuming that the former was fo-per buffered (MgO thin films) and the latter was fo-prEn buffered (quartz crucible). The global best fit incorporating the other studies requires a slightly higher activation energy. (b) shows the comparison between model and data, according to the global fit including the three studies. Most data fall within ±0.25 log units (dashed lines).

Figure 10: (a) The relationship between ionic radii and difference in diffusion coefficients between high $a\mathrm{SiO_2}$ (enstatite-buffered) and low $a\mathrm{SiO_2}$ (periclase buffered) for various elements where fully-buffered experiments have been conducted. Most data are at 1300 °C, or the closest temperature available. Al^{3+}: (Zhukova et al., 2017); Cr^{3+}, Cr^{2+}: (Jollands et al., 2018); Rh^{3+}: (Zhukova et al., 2018); Ni^{2+}, Co^{2+}: (Zhukova et al., 2018); Hf^{4+}, Zr^{4+}: (Jollands et al., 2014); Mg^{2+}:

this study; Y^{3+}: (Crépisson et al., 2012); Ca^{2+}: (Bloch et al., 2019). (b) Effect of $a SiO_2$ on diffusion as a function of site preference. Ni: M1 (Burns, 1970; Matsui and Syono, 1968); Co: M1 (Ghose and Wan, 1974); Ca^{2+}: M2 (Lumpkin et al., 1983; Mukhopadhyay and Lindsley, 1983); Cr^{2+}: M1 (Burns, 1970) or M2 (Li et al., 1995); Cr^{3+}: slight M1 preference (Petričević et al., 1988). Zr^{4+}, Hf^{4+}, REE^{3+}, Al^{3+}, Rh^{3+}: assumed to be ordered based on ionic radii for lack of quantitative data.

Table Captions

Table 1: Experimental conditions and results. Values of the quartz-fayalite-magnetite (QFM) equilibrium are from (O'Neill, 1987). Bold, italic values are from SHRIMP-RG, all others are from LA-ICP-MS. Values and uncertainties (1 s.d.) are weighted based on fit quality from ~five repeat profiles. *=reverse profile (see Figure 3). Note that these uncertainties likely underestimate the true uncertainty – this is described in more detail in the text. Missing data are usually due to profiles being too short to satisfactorily resolve, or issues with sample preparation leading to unrecoverable interfaces.

Table 2: Arrhenius parameters for fits to each condition (buffer+axis), calculated imposing different minimum uncertainties. Numbers in parentheses are 1σ. The bold values are the reduced chi squared closest to one from the different fits for each condition.

Supplementary Figure Captions

Supplementary Figure 1: Cartoon experimental and analytical procedure. 1) ~cubes of forsterite cut from a larger crystal, then polished on one face. Not shown: following cutting, forsterite was mounted in epoxy, ground and polished, then removed from the

878 resin. 2) Buffer powder, sintered then re-ground, was mixed with polyethylene oxide
879 glue, then pasted onto the crystal surface. The thickness was generally around 1 mm,
880 which decreases considerably when the glue is dried, then devolatilised at run
881 conditions. 3) Charge dried at 100 °C. 4) Diffusion experiment conducted in a tube or
882 box furnace, with conditions described in the text. 5) Following the experiment, the
883 charge was mounted in epoxy, and vacuum impregnated. This was often done with
884 several other charges in the same mount. Sometimes the buffering powder was
885 removed prior to mounting, other times it was not. 6) The mount was ground down on
886 a diamond wheel by at least 1mm, to expose the crystal core. Then, the mount was
887 diamond polished. 7) The sample was analysed by traversing a slit-shaped beam
888 across the surface, from core to rim (i.e. from low ^{26}Mg to high ^{26}Mg). Note: no depth
889 profiling was done in this study.

890 Supplementary Figure 2: Backscatter electron (BSE) images of the diffusion interface
891 and buffering powder taken post-experiment using an Oxford Instruments CamScan
892 scanning electron microscope (SEM) at the University of Lausanne. (a) fo-per
893 buffered experiment, showing laser tracks. (b) enlargement of (a), showing surface
894 roughness on the order of <10 μm. (c) and (d): as for (a) and (b), but for an enstatite-
895 buffered experiment. Note the longer laser tracks in (c) versus (a), given that
896 diffusivity is higher when buffered by fo-prEn compared to by fo-per.

897 Supplementary Figure 3: Comparison of diffusion coefficients (^{26}Mg) determined
898 following data reduction by the two methods. In both figures, the x axis is the
899 diffusion coefficient determined after normalising to ∑Mg, and the y axis is the
900 diffusion coefficient determined when the data are not normalised to ∑Mg. Reduced
901 chi-squared are calculated from a 1:1 correlation. (a) is determined using the depleting
902 interface solution (eq. (5)) and (b) using the fit to only part of the curve (eq. (4)).

Supplementary Figure 4: Extracted diffusion coefficients for ^{26}Mg versus ^{24}Mg, with uncertainties derived by combining the diffusion coefficients determined using the two fitting methods. Whilst the data cluster around the 1:1 line, the disagreement between diffusivities, and small uncertainties associated with ^{26}Mg, make the reduced chi squared too high to suggest a meaningful correlation.

Supplementary Figure 5: The effect of chosen interface position on the outputted logD values. (a) Example ^{29}Si and ^{26}Mg profiles, and the chosen interface position associated with a drop in ^{29}Si counts. (b) the effect of moving the interface in either direction on diffusion coefficients, and their uncertainties.

Supplementary Figure 6: Comparing the diffusivities extracted by fitting only the tail end of the diffusion profiles (partial fit) versus those determined using eq. (5), which assumes a linearly decreasing boundary condition. (a) histogram of the difference between Ds determined using the two methods, showing a mean offset to around -0.1 (i.e. the partial fit method gives Ds around 0.1 orders of magnitude lower than the depleting source method, when comparing medians). (b) all fits from the two methods, compared. Whilst the correlation appears strong, the reduced chi squared is extremely high, regardless of the fitting method used. This is because the errors from curve fitting are generally smaller than the discrepancy between Ds from the two methods.

Supplementary Figure 7: Considering the validity of eq. (5) to such a system as studied in this work. (a) schematic of the (1D) model used. A 0.1 mm thick buffer powder, with infinitely fast diffusion (no Mg isotopic gradient within the buffer at any time) and enriched ^{26}Mg, is attached to a 1 mm long crystal, with defined D and the natural abundance of ^{26}Mg. For simplicity we assume length is proportional to mass.

927 The model assumes no isotopic fractionation between buffer and crystal. All
928 modelling is done using an explicit finite difference approximation of Fick's second
929 law. (b) Comparison of the evolution of the boundary conditions over time. The
930 dashed line shows the linear decrease assumed by eq. (5), whereas the solid line
931 describes the evolution of the boundary when mass is conserved in the whole system,
932 with a shape close to logarithmic. This was calculated by subtracting the total amount
933 of ^{26}Mg in the crystal from the total ^{26}Mg in the whole system at every time step. (c)
934 Diffusion profiles generated using the two boundary conditions. The linear decrease
935 model predicts a slight inflexion in the near boundary, whereas the mass conservation
936 model does not. (d) The total amount of ^{26}Mg in the system (given as mean isotopic
937 ratio) over the duration of the model. The linear decrease boundary condition leads to
938 ^{26}Mg increasing then decreasing, which is clearly not feasible in a closed system.

939 Supplementary Figure 8: The relationship between uncertainties and diffusion profile
940 length. Uncertainties are calculated as described in the text, combining fits determined
941 using the two solutions to the diffusion equation, and incorporating the x0 term that
942 accounts for uncertainty on the interface position. The diffusion lengthscale is
943 calculated using the $4\sqrt{(Dt)}$ approximation, which is an estimate of the distance over
944 which the concentration decays by erf(2), i.e. by around 99.5%. (a) includes all fits,
945 (b) is the data after multiple fits have been combined.

946

947 Supplementary dataset 1: All ^{26}Mg profiles and fits. See the _README document for
948 more information.

Figure 1

(a)

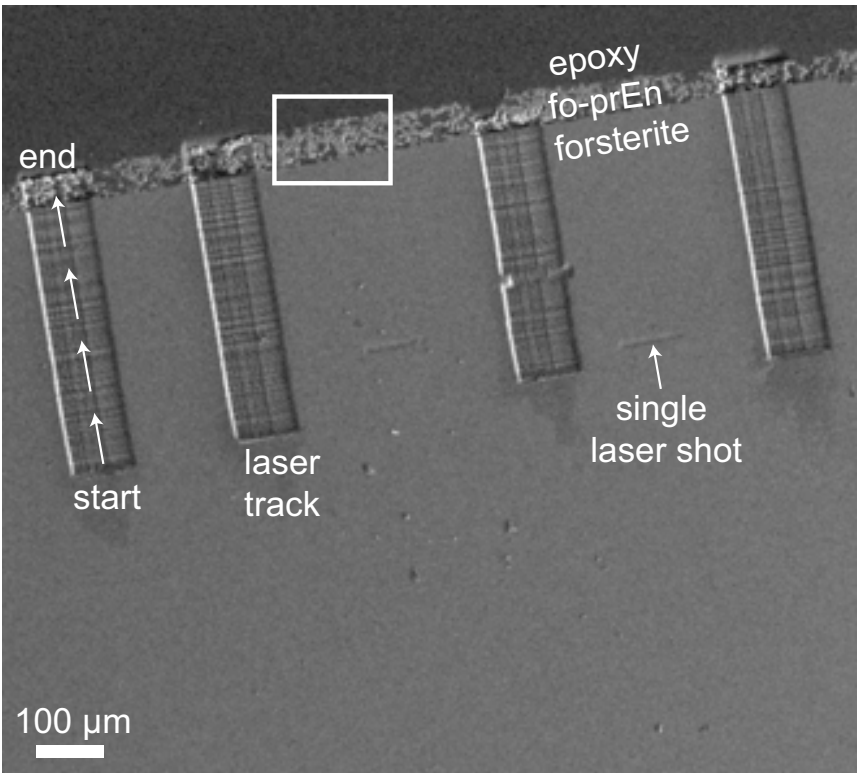
epoxy
fo-prEn
forsterite
end
start
laser
track
single
laser shot
100 µm

(b)

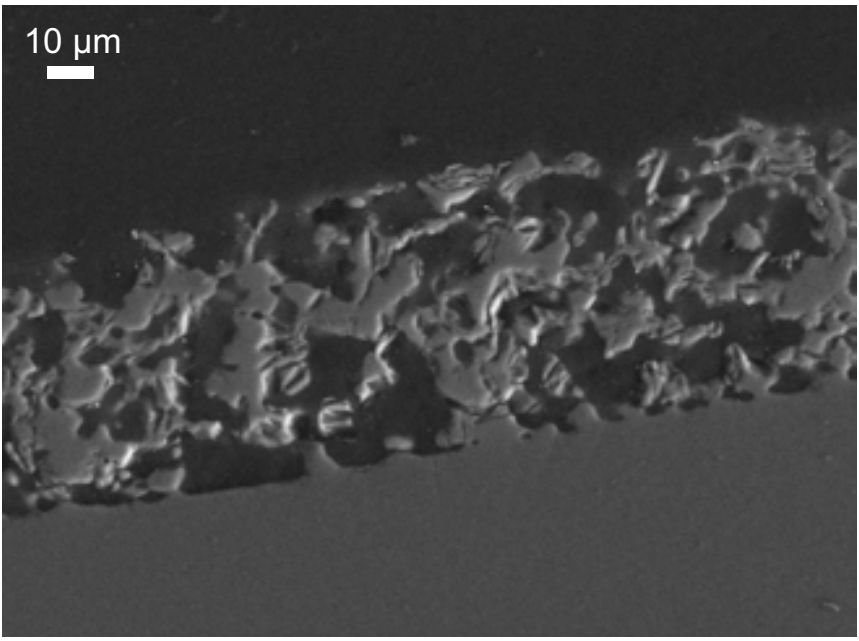
10 µm

Figure 2

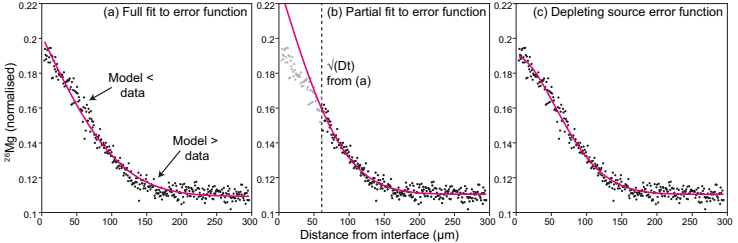
(a) Full fit to error function
(b) Partial fit to error function
(c) Depleting source error function
Model < data
Model > data
√(Dt) from (a)
^{26}Mg (normalised)
Distance from interface (μm)
0.22
0.2
0.18
0.16
0.14
0.12
0.1
0
50
100
150
200
250
300

Figure 3

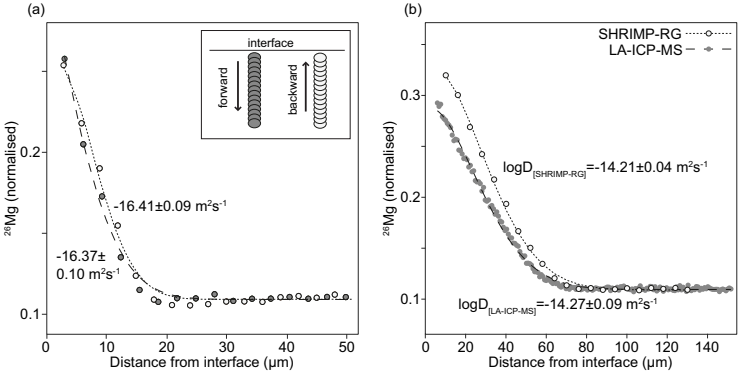
(a)
interface
forward
backward
-16.41±0.09 m²s⁻¹
-16.37±
0.10 m²s⁻¹
²⁶Mg (normalised)
Distance from interface (μm)
(b)
SHRIMP-RG
LA-ICP-MS
logD[SHRIMP-RG]=-14.21±0.04 m²s⁻¹
logD[LA-ICP-MS]=-14.27±0.09 m²s⁻¹
²⁶Mg (normalised)
Distance from interface (μm)

Figure 4

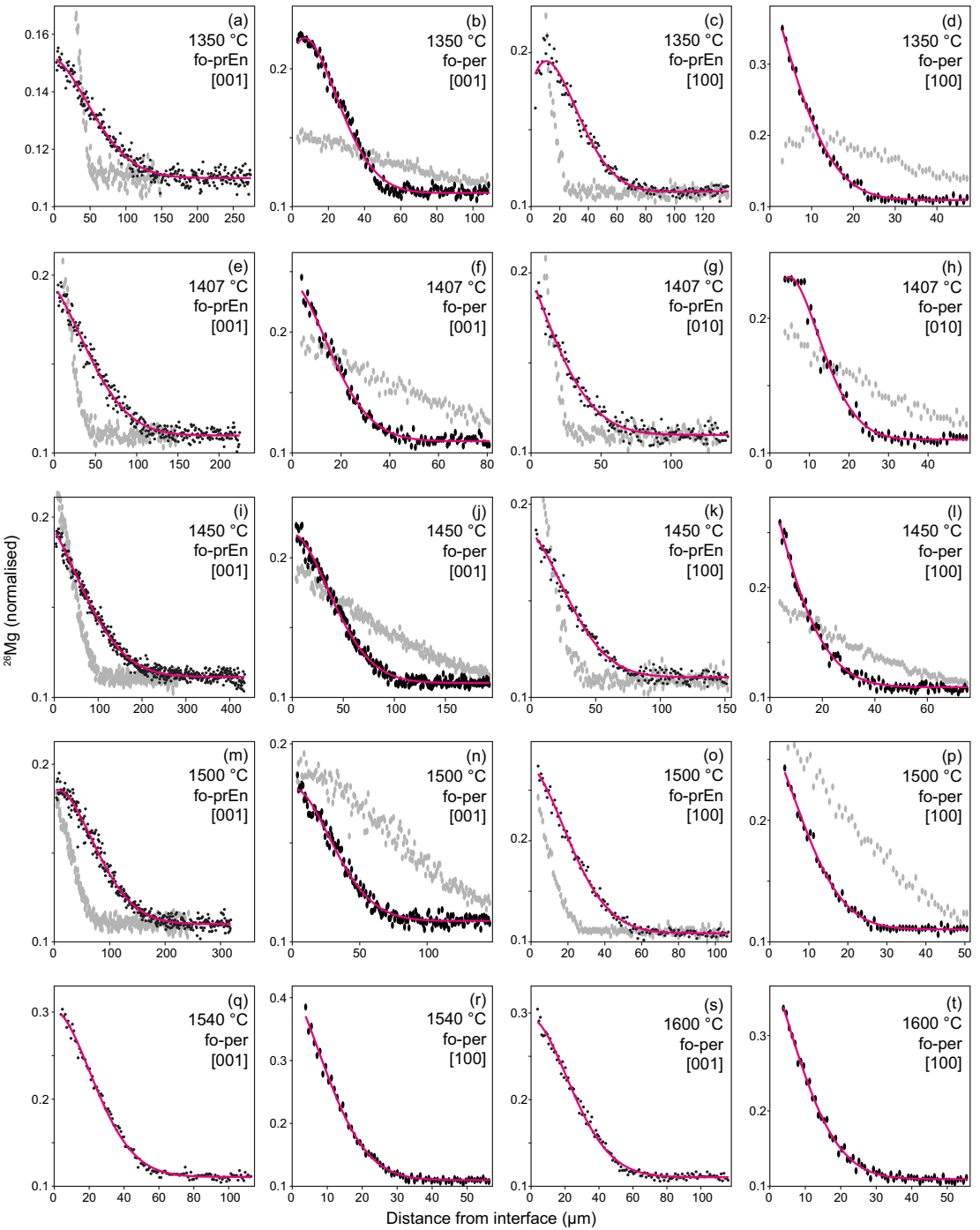
(a) 1350 °C fo-prEn [001]
(b) 1350 °C fo-per [001]
(c) 1350 °C fo-prEn [100]
(d) 1350 °C fo-per [100]
(e) 1407 °C fo-prEn [001]
(f) 1407 °C fo-per [001]
(g) 1407 °C fo-prEn [010]
(h) 1407 °C fo-per [010]
(i) 1450 °C fo-prEn [001]
(j) 1450 °C fo-per [001]
(k) 1450 °C fo-prEn [100]
(l) 1450 °C fo-per [100]
(m) 1500 °C fo-prEn [001]
(n) 1500 °C fo-per [001]
(o) 1500 °C fo-prEn [100]
(p) 1500 °C fo-per [100]
(q) 1540 °C fo-per [001]
(r) 1540 °C fo-per [100]
(s) 1600 °C fo-per [001]
(t) 1600 °C fo-per [100]
^{26}Mg (normalised)
Distance from interface (μm)

Figure 5

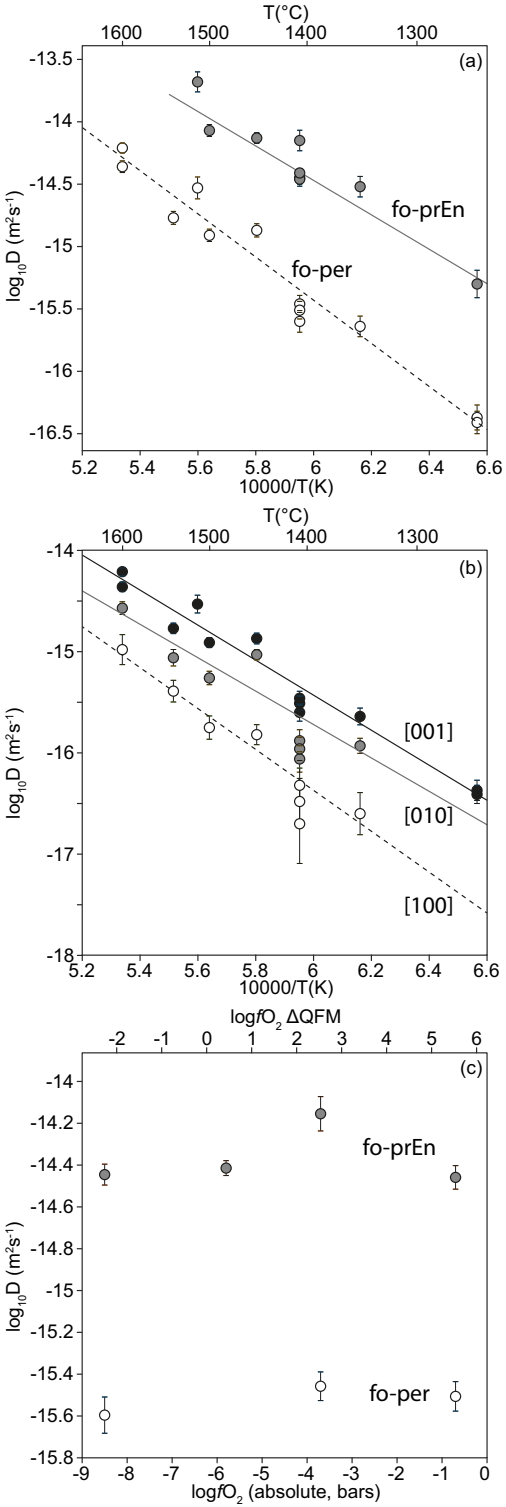
T(°C)
1600
1500
1400
1300
(a)
fo-prEn
fo-per
log10D (m2s-1)
10000/T(K)
(b)
[001]
[010]
[100]
logfO2 ΔQFM
(c)
logfO2 (absolute, bars)

Figure 6

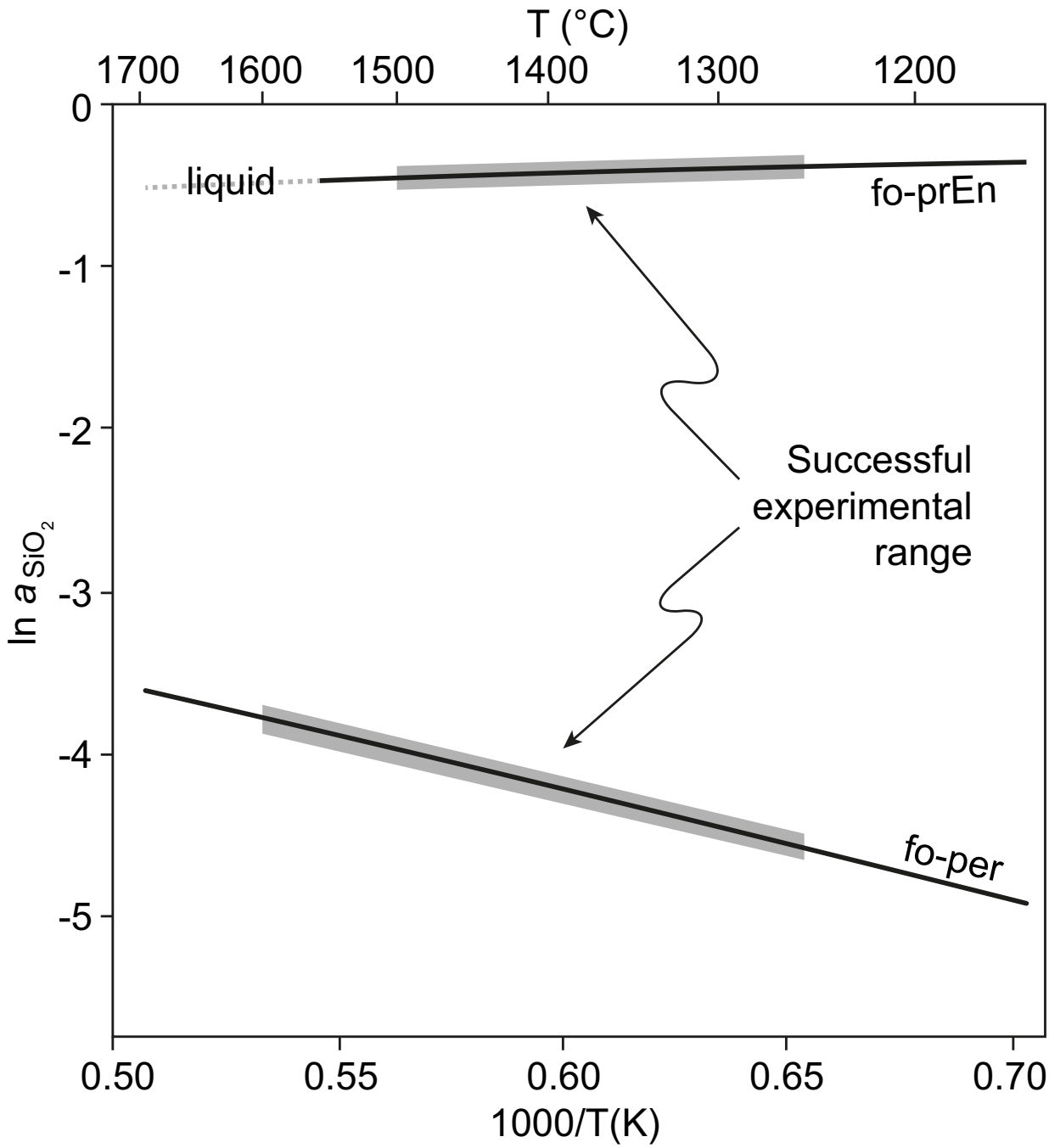
T (°C)
1700
1600
1500
1400
1300
1200
0
-1
-2
-3
-4
-5
ln a_{SiO_2}
liquid
fo-prEn
Successful
experimental
range
fo-per
0.50
0.55
0.60
0.65
0.70
1000/T(K)

Figure 7

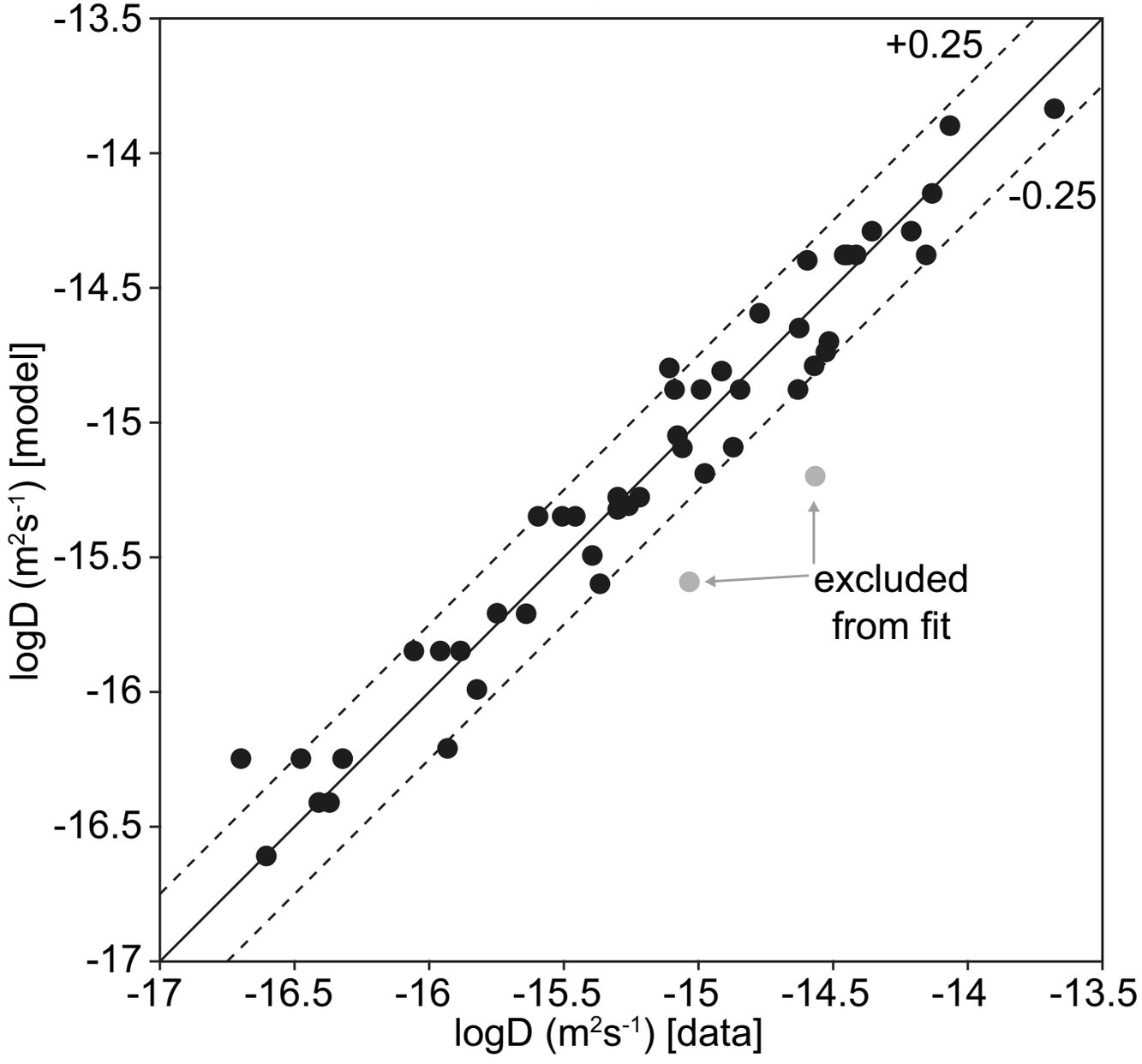
-13.5
-14
-14.5
-15
-15.5
-16
-16.5
-17
-17
-16.5
-16
-15.5
-15
-14.5
-14
-13.5
+0.25
-0.25
excluded
from fit
logD (m²s⁻¹) [model]
logD (m²s⁻¹) [data]

Figure 8

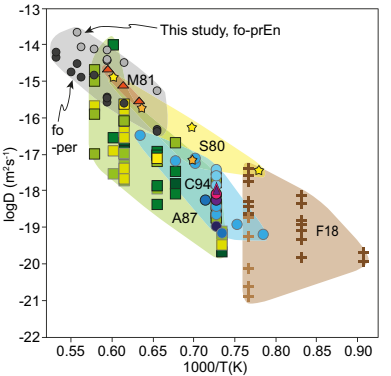

Chakraborty et al. (1994)
Fo1 (120-180 ppm Fe)
$MgSi_2O_6$
//[001], fO_2=10^{-12} bars
//[001], fO_2=10^{-6} bars
//[001], fO_2=$10^{-0.7}$ bars
MgO
//[001], fO_2=10^{-12} bars
//[001], fO_2=$10^{-0.7}$ bars
No buffer
//[100], fO_2=10^{-12} bars
//[010], fO_2=10^{-12} bars
//[001], fO_2=10^{-12} bars
//[001], fO_2=$10^{-0.7}$ bars
Fo2 (11 ppm Fe)
No buffer
//[001], fO_2=10^{-12} bars
//[001], fO_2=$10^{-0.7}$ bars

Sockel et al. (1980)
//[001], no buffer
//[010],[100], no buffer

Morioka (1981)
//[001], no buffer

Andersson (1987)
$MgSi_2O_6$
//[100]
//[010]
//[001]
MgO
//[100]
//[010]
//[001]

Fei et al. (2018)
'Wet', 8 GPa
'Dry', 1-13 GPa

Figure 9

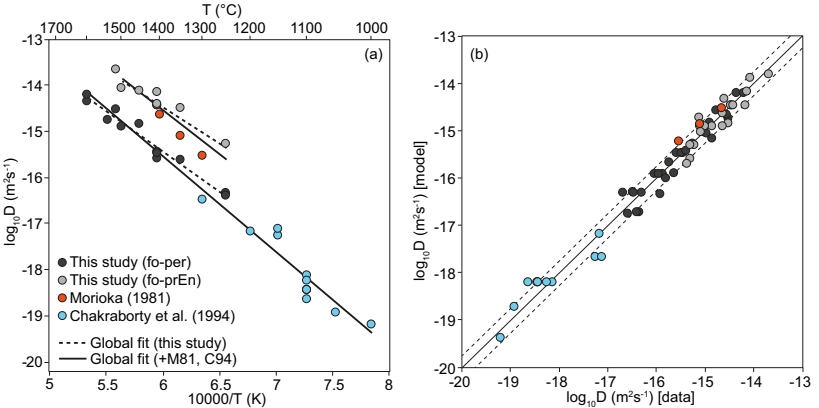
T (°C)
1700
1500
1400
1300
1200
1100
1000
(a)
log10D (m2s-1)
10000/T (K)
This study (fo-per)
This study (fo-prEn)
Morioka (1981)
Chakraborty et al. (1994)
Global fit (this study)
Global fit (+M81, C94)
(b)
log10D (m2s-1) [model]
log10D (m2s-1) [data]

Figure 10

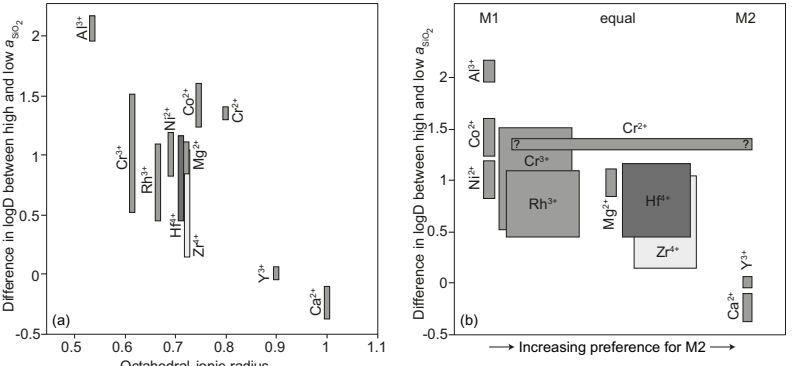
Difference in logD between high and low a_{SiO_2}
Octahedral ionic radius
(a)
Al^{3+}
Cr^{3+}
Rh^{3+}
Hf^{4+}
Zr^{4+}
Mg^{2+}
Ni^{2+}
Co^{2+}
Cr^{2+}
Y^{3+}
Ca^{2+}
M1
equal
M2
?
(b)
Increasing preference for M2

				$\log_{10} fO_2$ (bars)		$\log_{10} D(m^2 s^{-1})$		
		T (°C)	Time (s)	Absolute	ΔQFM	//[001]	//[010]	//[100]
Fo-prEn buffer	MFO14	1250	846720	-0.7	+7.1	***-15.30 (0.11)***		
	MFO9	1350	1200000	-0.7	+6.1	-14.52 (0.08)	-14.57 (0.08)	-15.37 (0.07)
	MFO12	1407	582240	-0.7	+5.5	-14.46 (0.06)	-15.09 (0.07)	
	MFO10	1407	678600	-8.5	-2-12.3	-14.45 (0.05)	-14.85 (0.05)	-15.22 (0.05)
	MFO11	1407	670500	-9.9	-3.7	-14.15 (0.08)	-14.63 (0.06)	
	MFO6	1407	773100	-12	-5.8	-14.41 (0.04)	-14.99 (0.05)	-15.3 (0.05)
	MFO3	1450	752400	-0.7	+5.1	-14.13 (0.04)	-14.63 (0.05)	-15.08 (0.05)
	MFO13	1500	372000	-0.7	+4.7	-14.07 (0.05)	-14.6 (0.05)	-15.11 (0.06)
	MFO1	1513	489600	-0.7	+4.6	-13.68 (0.08)		
Fo-per buffer	MFO14	1250	846720	-0.7	+7.1	***-16.37 (0.10)*** ***-16.41 (0.09)****		
	MFO9	1350	1200000	-0.7	+6.1	-15.64 (0.08)	-15.93 (0.07)	-16.6 (0.21)
	MFO12	1407	582240	-0.7	+5.5	-15.51 (0.07)	-15.96 (0.11)	-16.48 (0.23)
	MFO10	1407	678600	-8.5	-2.3	-15.6 (0.09)	-15.88 (0.11)	-16.32 (0.17)
	MFO11	1407	670500	-9.9	-3.7	-15.46 (0.07)	-15.88 (0.11)	-16.7 (0.39)
	MFO3	1450	752400	-0.7	+5.1	-14.87 (0.05)	-15.03 (0.05)	-15.82 (0.1)
	MFO13	1500	372000	-0.7	+4.7	-14.91 (0.05)	-15.26 (0.07)	-15.75 (0.11)
	MFO1	1513	489600	-0.7	+4.6	-14.53 (0.09)		
	MFO7	1540	172800	-0.7	+4.4	-14.77 (0.05)	-15.06 (0.08)	-15.39 (0.11)
	MFO8	1600	86400	-0.7	+3.9	-14.36 (0.05) ***-14.21 (0.04)***	-14.57 (0.06)	-14.98 (0.15)

		Using σ from Table 1			σ_{min} = 0.1			σ_{min} = 0.2			T range
Axis	**Buffer**	**E_a**	**logD0**	χ_v^2	**E_a**	**logD0**	χ_v^2	**E_a**	**logD0**	χ_v^2	
//[001]	fo-prEn	264 (19)	-6.2 (0.6)	4.3	279 (25)	-5.7 (0.8)	**2.0**	281 (47)	-5.6 (1.5)	**0.5**	1250-1513
//[001]	fo-per	334 (10)	-5.0 (0.3)	8.6	332 (14)	-5.1 (0.4)	4.0	332 (28)	-5.1 (0.9)	**1.1**	1250-1600
//[010]	fo-prEn	97 (28)	-11.8 (0.9)	13.2	39 (49)	-13.6 (1.5)	5.2	39 (98)	-13.6 (3.0)	**1.3**	1350-1500
//[010]	fo-per	315 (20)	-5.8 (0.6)	13.4	340 (27)	-5.1 (0.8)	6.0	354 (53)	4.8 (1.6)	**1.7**	1350-1600
//[100]	fo-prEn	110 (30)	-11.8 (0.9)	2.5	113 (49)	-11.8 (1.5)	1.7	125 (98)	-11.4 (3.0)	**1.4**	1350-1500
//[100]	fo-per	386 (44)	-4.3 (1.3)	**0.92**	387 (44)	-4.2 (1.3)	0.91	399 (55)	-3.9 (1.7)	0.51	1350-1600